Geomechanics and Engineering, *Vol. 38, No. 3 (2024) 285-305*
https://doi.org/10.12989/gae.2024.38.3.285

Analytical and ANN-based models for assessment of hunchback retaining walls: Investigating lateral earth pressure in unsaturated backfill

Sivani Remash Thottoth* and Vishwas N Khatri[a]

Department of Civil Engineering, IIT(ISM) Dhanbad, Jharkhand, 826004, India

(*Received May 4, 2024, Revised July 21, 2022, Accepted July 23, 2024*)

Abstract. This study investigates the behaviour of hunchback retaining walls supporting unsaturated sandy backfill under active earth pressure conditions. Utilizing a horizontal slice method and a unified effective stress methodology, the influence of various factors on lateral earth pressure, including the position of the hunch along the wall, friction angles, and wall heights, is explored. The results suggest that relocating the hunch position from close to the wall's top to near its base leads to a significant decrease (ranging from 54% to 81%) in lateral earth pressure. However, as the hunch position transitions from near the top to mid-height, the point of application of active thrust shifts upward initially, then slightly downward as the hunch position approaches the toe. Notably, the reduction in lateral earth pressure is more pronounced for shorter wall heights and higher friction angles. Building upon these findings, an Artificial Neural Network (ANN)-based model is developed to accurately predict the lateral earth pressure coefficient and point of application, achieving R^2 values of 0.94 and 0.93, respectively. In addition, an analytical model based on Coulomb's earth pressure theory is presented and compared with ANN models. These models are anticipated to assist designers and practitioners in optimizing hunchback retaining walls for unsaturated backfill.

Keywords: ANN; hunch back wall; method of horizontal slices; unsaturated soil

1. Introduction

Retaining walls are critical structural elements that have been extensively investigated from a geotechnical perspective. A significant amount of research has focused on both the static and seismic analysis of earth pressure, considering dry, unsaturated, and saturated backfill retained by both reinforced and unreinforced walls (Fathipour *et al.* 2021a, b, c, Mirmoazen *et al*. 2021, 2022, Payan *et al.* 2022). However, the bi-linearity of the wall back face has received significantly less attention (Kolathayar and Ghosh 2009, 2011, Rahaman and Raychowdhury 2017).

Among bilinear back face walls, hunchback retaining walls, commonly employed as quay walls for waterfront structures, play a pivotal role in effectively managing lateral earth pressure and adapting to diverse site conditions. This design incorporates both outward-leaning and landward-leaning facets, aiming to balance earth pressure distribution (Sadrekarimi *et al*. 2008, Sadrekarimi 2010). Compared to traditional vertical walls, this innovative design optimizes force distribution, enhancing overall stability and cost-effectiveness. A study by Santhoshkumar and Ghosh (2020), using the stress characteristics method, reaffirmed the efficacy of hunchback walls in terms of improved stability during static and seismic analyses. However, it is noteworthy that existing studies on hunchback retaining walls assumed a completely dry backfill, neglecting the potential impact of partial saturation of the backfill soil above the water table on lateral earth pressure.

In this context, soil strength in an unsaturated state is typically estimated using the total stress approach proposed by Fredlund *et al.* (1978). This method utilizes two independent stress variables: net normal stress (σ-u_a) and matric suction (u_a-u_w), where σ represents total normal stress, and u_a and u_w indicate pore air pressure and pore water pressure, respectively. Matric suction is incorporated into the model through a component of the internal friction angle known as ϕ_b, which requires extensive and time-consuming laboratory testing, thereby limiting the practicality of this approach.

Alternatively, the effective stress approach by Bishop (1959) employing a single stress parameter χ is utilized to estimate soil strength. The parameter χ has a value of one when the soil is fully saturated and zero when it is completely dry. The main advantage of this method is that it allows for the complete characterization of soil strength using a single stress parameter rather than two or three independent stress state variables. However, accurately estimating χ remains a challenge.

Lu and Likos (2006) introduced the concept of suction stress within the effective stress framework to address these limitations. In their work, macroscopic pore pressure is broken down into various microscopic interparticle forces within the soil grain matrix, including van der Waals, electrical double-layer, cementation, surface tension, and forces from negative pore water pressure. These forces are combined into the macroscopic 'suction stress,' which depends on the degree of saturation, water content, or matric suction, as described by the suction stress characteristic curve (SSCC) proposed by Lu and Likos

*Corresponding author, Ph.D. Student
E-mail: sivaniremasht@gmail.com
[a]Associate Professor

ISSN: 2005-307X (Print), 2092-6219 (Online)

(2006).

This model calculates matric suction and associated stresses, considering diverse soil types, seepage conditions, and other geotechnical properties. As an illustration, *Lu et al.* (2010) presented a closed-form solution to evaluate effective stress in unsaturated soils, incorporating the van Genuchten soil water characteristic curve model and the prevailing flow conditions. This methodology has been utilized in a range of stability issues, including: (i) determining lateral earth pressure (Zhao *et al.* 2009, Zhang *et al.* 2010, Stanier and Tarantino 2010, Liang *et al.* 2012, Vo and Russell 2014, Vahedifard *et al.* 2015, Sahoo and Ganesh 2018, Li and Yang 2019; Shahrokhabadi *et al*. 2019b; Fathipour *et al.* 2020, Yang and Chen 2021, Abdollahi *et al.* 2021, Rajesh and Ganesh 2022, Bahmani Tajani *et al.* 2023), (ii) assessing the bearing capacity of shallow foundations (Nouzari *et al.* 2021a, Chenari *et al.* 2023, Fathipour *et al.* 2023a,b, Maghferati *et al.* 2023), and (iii) estimating slope stability (Wang *et al.* 2019, 2020). In the context of current research on earth pressure determination involving unsaturated backfill, relevant studies are highlighted below.

For instance, Sahoo and Ganesh (2018) investigated tension crack depth in retaining walls due to unsaturated backfill, employing limit equilibrium and using a linear failure wedge. Li and Yang (2019) and Shahrokhabadi *et al.* (2019) focused on analyzing active earth pressure under steady and transient flow conditions in unsaturated soils. Additional studies applied limit analysis principles and the concept of effective suction stress to assess earth pressures, considering scenarios such as passive earth pressure in unsaturated soils (Zhao *et al.* 2009), the collapse of cohesionless soils above the water table (Stanier and Tarantino 2010), and the earth pressure on vertical walls supporting unsaturated backfill (Fathipour *et al.* 2020). Similarly, Yang and Chen (2021) introduced a numerical procedure utilizing upper bound limit analysis to estimate seismic earth pressures for three-dimensional unsaturated backfill. Fathipour *et al*. (2022) conducted an extensive study on the effect of transient flow on matric suction, highlighting its significant impact on cohesive soils. Bahmani Tajani *et al.* (2023) explored the influence of elevated temperatures on lateral earth pressures in partially saturated soils, indicating that unsaturated sand backfill was less susceptible to temperature changes compared to clayey backfill.

Although extensive research has been conducted on estimating earth pressure on vertical retaining walls with unsaturated backfill conditions, there is a notable lack of studies concerning hunchback walls. Furthermore, there are few investigations into the point of application of active thrust for non-vertical retaining walls. This study aims to fill this gap.

The present study investigates the variation in active earth pressure and failure patterns for a hunchback retaining wall supporting unsaturated backfill. The analysis utilizes the horizontal slice method and a unified effective stress approach to account for the unsaturation effects in the backfill soil. Researchers have widely used the horizontal slice methodology to address various geotechnical stability problems (Ghanbari and Ahmadabadi 2010, Chandaluri *et al.* 2015, Nouzari *et al.* 2021b, Afsharpour *et al.* 2022, Agarwal *et al*. 2022, Aroni Hesari *et al.* 2022, Fatehi *et al.* 2023) due to its effectiveness in providing reliable solutions. It is important to note that, except for Nouzari *et al*. (2021), all the aforementioned literature pertains to dry backfills. This emphasizes the use of the horizontal slice method for applications in unsaturated backfills. Notably, utilizing the horizontal slice method enables the consideration of varying suction stress across the soil depth and facilitates the incorporation of nonlinear failure surfaces.

Accordingly, this methodology has been adopted to analyze the variation in the active earth pressure coefficient (K_a) as well as the point of application ($\bar{z}$) of active thrust behind the wall under different conditions, including i) varying hunch positions along the wall height and ii) different hunch angles. Additionally, acknowledging the complexities involved in estimating K_a and $\bar{z}$, particularly given the presence of a hunch at the back of the wall and the consideration of unsaturated backfill, a predictive model is developed using Artificial Neural Network (ANN) techniques, relying on numerical outcomes.

Notably, Machine Learning (ML) models, such as Artificial Neural Networks (ANN), operate based on data, enabling them to discern complex nonlinear relationships between input and target variables without strict assumptions. Accordingly, soft computing techniques have gained prominence in addressing various geotechnical problems (Xiao and Zhao 2019, Nguyen *et al.* 2020, Raja and Shukla 2021a, b, Bardhan *et al.* 2021, Khan *et al*. 2021, Kardani *et al.* 2022, Raja *et al.* 2022, Ngamkhanong *et al.* 2022, Das and Khatri 2022, Khodkari *et al.* 2024, Thottoth *et al.* 2024a, Menon and Kolathayar 2024, Khoshdel Sangdeh *et al.* 2024). However, there has been limited research on effective prediction models for earth pressure coefficients that consider the effects of unsaturation on retaining walls, particularly hunchback walls.

This study seeks to bridge this gap by utilizing artificial neural networks (ANN) to establish relationships between input parameters, such as the geometry of hunchback walls and soil properties, and output parameters, including the earth pressure coefficient and the point of application of the active thrust. Additionally, a sensitivity analysis is conducted on the optimized model to explore the impact of each input parameter on the output.

In addition to the ANN prediction model, an analytical method to calculate active earth pressure on the hunchback wall is devised employing Coulomb's earth pressure theory. This model is then contrasted with the ANN model to evaluate their effectiveness and to suggest an optimal approach.

It is intended that both these models will aid practitioners in the design and analysis of hunchback retaining walls with unsaturated backfill.

2. Problem domain

Fig. 1(a) illustrates a rigid retaining wall of height 'h' with a hunched back supporting partially saturated cohesionless soil. The wall height in the study varied between 4 m to 10 m. The base width of the wall is denoted

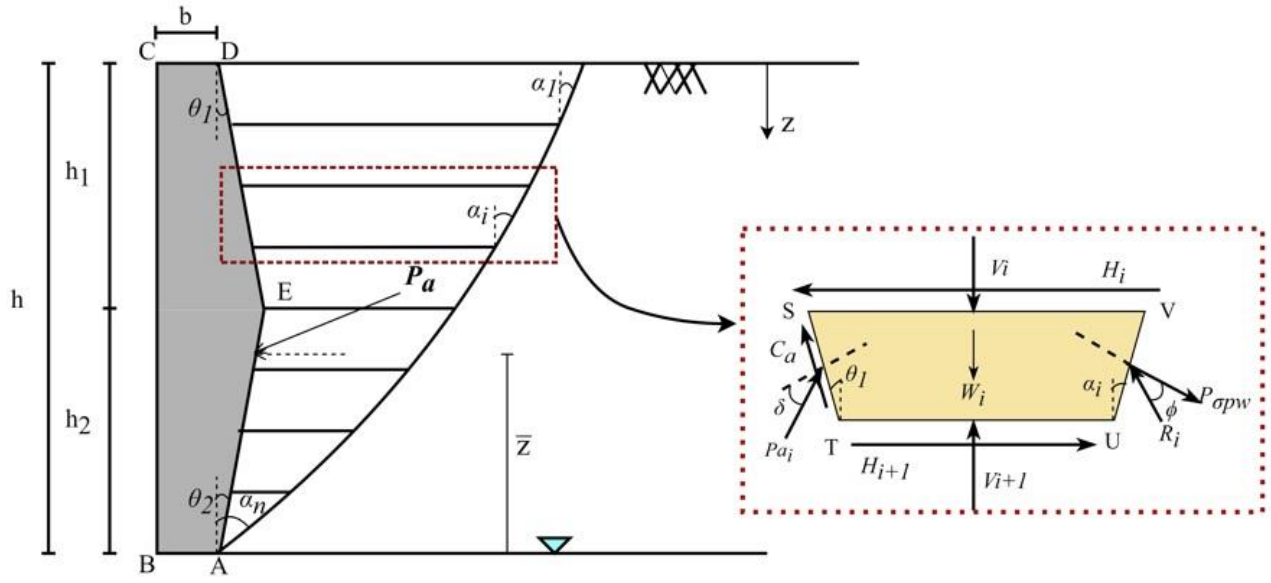

(a) (b)

Fig. 1 Soil domain adopted for the present study

by the parameter 'b'. For the sake of analysis, the retaining wall is divided into two distinct sections: an upper portion (DE) with a height of h_1, inclined at an angle θ_1° relative to the vertical, and a lower portion (AE) with a height of h_2, inclined vertically at an angle θ_2°. The hunch position (h_1/h) along the retaining wall is determined by the hunch angles θ_1 and θ_2. This study examined the hunch position (h_1/h) at 1/3, 1/2, and 2/3. Accordingly, the h_1/h_2 ratio at these hunch positions for given θ_1 can be determined as 0.5, 1, and 2.

It should be noted that for h_1/h_2 =0.5, the hunch angle θ_1 was varied between 5°-20°, while the θ_2 for given value of θ_1 was calculated as

$$\theta_2 = \tan^{-1}\left[\frac{h_1}{h_2}\tan\theta_1\right] \quad (1)$$

Conversely, for h_1/h_2 =2, the hunch angle θ_2 was varied between 5°-20°, while the θ_1 for given value of θ_2 was determined as:

$$\theta_1 = \tan^{-1}\left[\frac{h_2}{h_1}\tan\theta_2\right] \quad (2)$$

With this consideration, the magnitude of θ_1 and θ_2 corresponding to the selected hunch position is depicted in Table 1. Note that θ_1= θ_2=0 indicates a vertical retaining wall without any hunch.

The top surface of the backfill is assumed horizontal with a unit weight of γ and a friction angle of ϕ. The soil-wall interface friction angle (δ) was varied between 0-ϕ, respectively, to distinguish between smooth and rough walls. The water table is presumed to be located at the toe of the wall.

The soil mass behind the wall is divided into n horizontal strips or slices, each with a thickness (Δh) calculated as h/n. It is essential to emphasize that the failure surface in this study is not pre-defined. Instead, it is assumed to comprise horizontal slices inclined at an angle of α_i to the vertical, where i varies from 1 to n. The force equilibrium of a slice, along with other pertinent equations, is described below.

Table 1 Details of hunch back wall geometry

Hunch Position	h_1/h_2	θ_1	θ_2
At the top (@ h/3)	1/2	5	2.5
		10	5
		15	7.6
		20	10.3
At the middle (@ h/2)	1	5	5
		10	10
		15	15
		20	20
At the bottom (@ 2h/3)	2	2.5	5
		5	10
		7.6	15
		10.3	20

3. Formulation

The problem formulation involves determining interslice forces and pore water pressure in an unsaturated state. Subsequently, the equilibrium of forces is applied to ascertain the active thrust (P_a) and the lateral earth pressure coefficient (K_a). The following paragraphs elaborate on each step of this process.

3.1 Determination of horizontal and vertical interslice forces

In the analysis, each slice is subjected to vertical

interslice forces V_i and V_{i+1} and horizontal interslice forces H_i and H_{i+1} acting on the top and bottom edge of slices (Fig.1(b)). W_i denotes the weight of each slice. The vertical interslice force V_i or V_{i+1} is determined by multiplying the slice with the vertical pressure on the top of the horizontal edge of a given slice (Shahgholi *et al.* 2001) that is $V_i = (q_s+\gamma z)l_i$, where q_s indicate surcharge on the topmost slice, z represents depth from ground level, and l_i is the length of the top edge of i^{th} slice (Chandaluri *et al.* 2015, Dey *et al.* 2017). In this study, the top of the backfill was assumed to be free of any surcharge, resulting in the value of q_s being set to zero. Meanwhile, the horizontal component (H_i or H_{i+1}) of the interslice force was computed using the following relationship

$$H_i = V_i \tan(k\phi) \quad (3)$$

Note that in the previously reported studies (Ghanbari and Ahmadabadi 2010; Chandaluri *et al.* 2015; Farshidfar *et al.* 2020; Agarwal *et al.* 2022), the coefficient k was assumed to be equal to 1, indicating adherence to Mohr-Coulomb's failure criterion. However, in the present study, the coefficient k is optimized within the range of 0 to 1 to achieve the maximum value of the active earth thrust.

3.2 Determination of pore water pressure and associated forces

Lu and Likos (2006) introduced the notion of suction stress, considering inter-particle forces, which include van der Waals, capillary, and electrical double-layer attraction and repulsion forces acting among air-water, air-soil, and water-soil particles. Building upon this, Lu *et al.* (2010) extended the concept by incorporating the van Genuchten Soil Water Characteristic Curve (SWCC), Gardner's hydraulic conductivity function, and Darcy's law. As a result, the following expression for σ_{pw} is formulated for a point above the water table:

$$\sigma_{pw} = \frac{1}{\alpha_a} \frac{\ln\left[\left(1+\frac{q}{k_s}\right)e^{-\gamma_w \alpha_a (h-z)} - \frac{q}{k_s}\right]}{\left(1+\left\{-\ln\left[\left(1+\frac{q}{k_s}\right)e^{-\gamma_w \alpha_a (h-z)} - \frac{q}{k_s}\right]\right\}^{n_p}\right)^{(n_p-1)/n_p}} \quad (4)$$

Note that the distance (h-z) in the above equation corresponds to the vertical distance from the bottom of the wall to the centre of a given slice, α_a is the reciprocal of the air entry pressure, k_s is the hydraulic conductivity for the saturated soil mass, q is the flow parameter, γ_w is the unit weight of water and n_p is the pore size spectrum number.
It is important to note that the parameters α_a and n_p are solely dependent on the soil type, with values within the range of 0 to 0.5 $kPa^{-1}$and 1.1 to 8.5, respectively (Lu and Likos 2006, Vahedifard *et al.* 2015, Fathipour *et al.* 2020). Furthermore, flow conditions do not significantly affect suction stress distribution for cohesionless soil (Lu and Griffiths 2004, Lu and Likos 2006, Vahedifard *et al.* 2015, Fathipour *et al.* 2020). Hence, q = 0 can be substituted in Eq (4). This study uses n_p = 5 and α_a = 0.1 kPa^{-1} to determine the magnitude of σ_{pw} (Fathipour *et al.* 2020, Vahedifard *et al.* 2015). Accordingly, the suction stress profiles obtained using Eq. (4) are depicted in Fig. 2

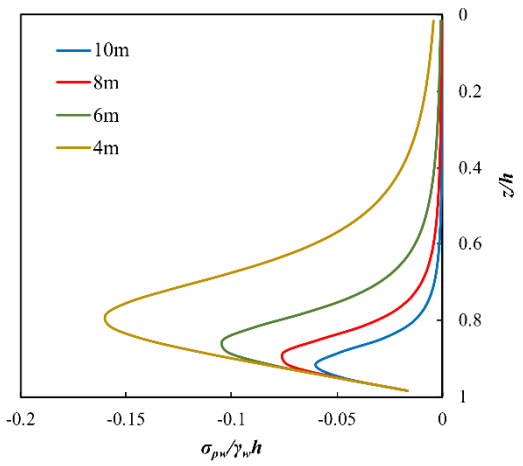

Fig. 2 Suction stress profile considered for analysis

For clarity in interpretation, the suction stress (σ_{pw}) has been normalized by dividing it by (γ_wh). Upon analyzing Fig. 2, it is apparent that the suction stress (σ_{pw}) displays a markedly nonlinear behaviour. As one progresses upwards from the base of the wall, the magnitude of suction stress increases to a maximum at a certain distance. Beyond this level, it decreases, ultimately reaching zero, signifying a dry soil region. For the range of wall heights considered in the analysis, from 4 m to 10 m, the maximum suction stress occurs when the z/h is between 0.75 and 0.9, while the point where suction stress becomes negligible can be identified at z/h= 0.2 to 0.4.

By utilizing the magnitude of σ_{pw}, the normal force $P_{\sigma pw}$ acting on the right edge of the slice (refer to Fig 1(b)) can be estimated by multiplying it with the length of the edge. Contrary to the right edge, the effect of pore water pressure along the wall is considered using a pseudo-adhesion (c_a) given by -σ_{pw} tan δ (Lu *et al.* 2010, Vahedifard *et al.* 2015), wherein δ represents the soil-wall interface friction angle defined earlier. Accordingly, the pseudo-adhesive force (C_a) can be estimated by multiplying the pseudo-adhesion with the left edge of a given slice (refer to Fig 1(b)). Notably, a negative value of σ_{pw} (suction) augments the shear strength, whereas a positive value diminishes the shear strength as per the effective stress principle (Terzaghi 1943).

It is important to note that this study assumes a steady-state flow condition, which is time-independent. If time-dependent transient flow is to be considered, a different closed-form solution, like the one proposed by Richards (1931), should be employed. In such cases, the suction stress in transient flow can vary with time, potentially being higher or lower than in steady-state flow (Fathipour *et al.* 2022). This variation results in time-dependent shear strength, affecting the active earth pressure generated by the backfill against the wall.

3.3 Determination of active earth pressure (P_a) and coefficient of active earth pressure (K_a)

The system of forces acting on an individual slice

represented in Fig. 1(b) is resolved using the equilibrium equations, and a final expression of the active thrust (P_{ai}) of the i^{th} slice is arrived at as follows

$$\sum F_x = 0;\ P_{ai}\cos(\theta+\delta) - R_i\cos(\alpha_i+\phi) + P_{\sigma pw}\cos\alpha_i + H_i - H_{i-1} + C_a\, sin\theta = 0 \quad (5a)$$

$$\sum F_y = 0;\ W_i - P_{ai}\sin(\theta+\delta) - R_i\sin(\alpha_i+\phi) + P_{\sigma pw}\sin\alpha_i + V_{i-1} - V_i + C_a\cos\theta = 0 \quad (5b)$$

Solving the above equations (Eq. 5(a) and 5(b)), the following expression for P_{ai} is arrived at

$$P_{ai} = \frac{(W_i + V_{i-1} - V_i)\cos(\alpha_i+\phi) + (H_{i-1} - H_i)\sin(\alpha_i+\phi) - P_{\sigma pw}\sin\phi + c_a\Delta h\frac{\cos(\theta+\alpha_i+\phi)}{\cos\theta}}{\sin(\theta+\delta+\phi+\alpha_i)} \quad (6)$$

The hunch angle, θ, is taken as θ_1 in the upper part (DE) and θ_2 in the lower part (AE) of the hunchback wall. Using Eq. (6), the active thrust for each slice in the upper (DE) and lower (AE) portions of the hunch back wall can be calculated by substituting θ_1 and θ_2 in place of θ. Thus, the total active thrust can be obtained as follow

$$P_a = \sum_{i=1}^{n} P_{ai} \quad (7)$$

Subsequently, the active earth pressure coefficient K_a can be defined as:

$$K_a = \frac{2P_a}{\gamma H^2} \quad (8)$$

Evidently, P_a depends on α and k. The maximum value of P_a is achieved by optimizing Eq. (8) concerning α_i and k. The resulting nonlinear constrained optimization problem was solved by developing a MATLAB code and employing the library program *fmincon*. During optimization, the wedge angle α_i was allowed to fluctuate within bounds of 0° to 90°, while the coefficient k varied between 0 to 1.

Once the P_a is calculated, the point of application of the active thrust can be obtained by taking the moment about toe of the wall. The distance to the point of application ($\bar{z}$) from the toe of the wall is normalized with wall height for generalization of results.

3.4 Development of ANN model

This investigation employs an Artificial Neural Network (ANN) model, a computational framework for data-driven learning and prediction (Zurada 1992, Reeves 1993, Fausett 1994). It consists of layers of artificial neurons; the input layer captures raw data, while subsequent hidden layers transform the information to discern meaningful patterns and relationships. The output layer synthesizes processed information, and the iterative adjustment of weights and biases refines the network through learning and adaptation to data patterns. This refinement process involves continuous comparison of desired targets with predictions and evaluating errors over time. The performance of the ANN model is contingent upon factors such as the training dataset, neural network architecture, and the selection of training functions, all of which are detailed in the following sections.

Table 2 Input and output parameters used in the study

	Parameter	Min	Max	Mean	SD
Input	Height of wall, h (m)	4	10	6.972	2.219
	Top hunch angle, θ_1 (°)	0	20	9.804	6.078
	Bottom hunch angle, θ_2 (°)	0	20	9.804	6.078
	Internal friction angle, ϕ (°)	20	45	32.082	8.329
	Interface friction, δ/ ϕ	0	1	0.495	0.338
Output	Earth pressure coefficient, K_a	0.021	0.484	0.228	0.099
	Point of application of earth pressure, $\bar{z}$	0.277	0.909	0.387	0.050

3.4.1 Dataset

The selection of input parameters for the model is driven by their significance in estimating the active earth pressure coefficient (K_a) and point of application of pressure ($\bar{z}$) for a hunchback retaining wall supporting an unsaturated backfill. The chosen input parameters include (i) wall height (h), (ii) hunch angle at the top portion of a wall (θ_1), (iii) hunch angle at the bottom portion of a wall (θ_2), (iv) soil friction angle (ϕ) and (v) normalized soil-wall interface friction (δ/ϕ). Table 2 outlines the range of input values along with their standard deviations (SD). A total of 1367 datasets were generated employing the numerical method described above to establish a robust and highly efficient ANN model. In accordance with findings in the literature (Kuo *et al.* 2009, Kalinli *et al.* 2011, Momeni *et al.* 2015, Acharyya *et al.* 2020, Hasthi *et al.* 2022), 80% of the data was allocated for network training, while the remaining 20% served as testing data.

3.4.2 Neural architecture

The model comprises one input layer corresponding to the investigated input parameters, one hidden layer, and one output layer representing the output variables K_a and $\bar{z}$. The input layer had five nodes, each corresponding to an input parameter. The number of nodes in the hidden layer is chosen carefully to balance the model's ability to approximate desired functions while preventing overfitting and minimizing error. It was achieved by training the network multiple times and employing different numbers of hidden neurons using the Levenberg-Marquardt training method. The Hyperbolic Tangent function (tanh(x)) serves as the activation function for the hidden layer neurons, as described in Eq. (9). The output node utilizes the Linear Transfer function. The predicted output follows the structure in Eq. (10), where W represents connection weights, b_a is the bias, N_h is the number of hidden neurons, x is the input parameter, and J is the number of input parameters.

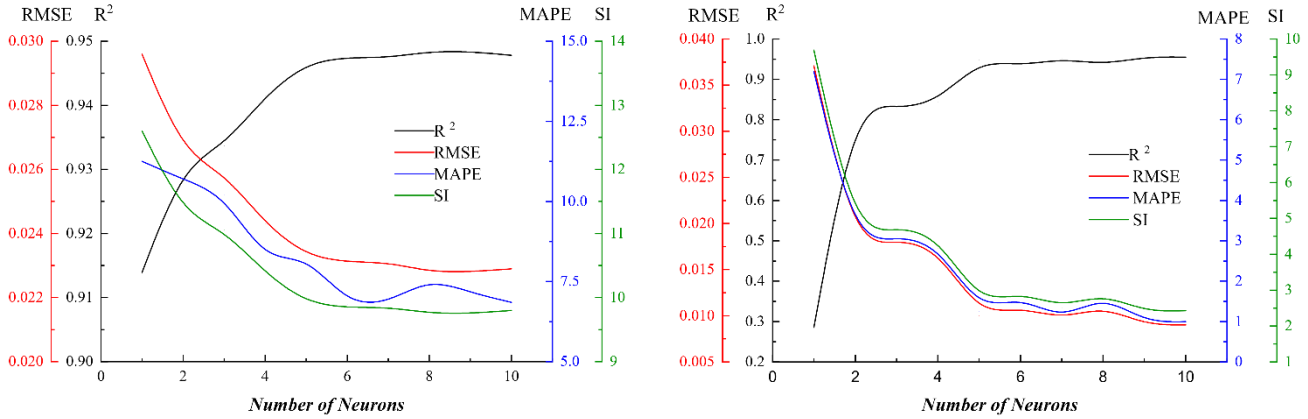

(a) Active earth pressure coefficient, K_a (b) point of application of earth pressure, $\bar{z}$

Fig. 3 Number of neurons versus error parameters

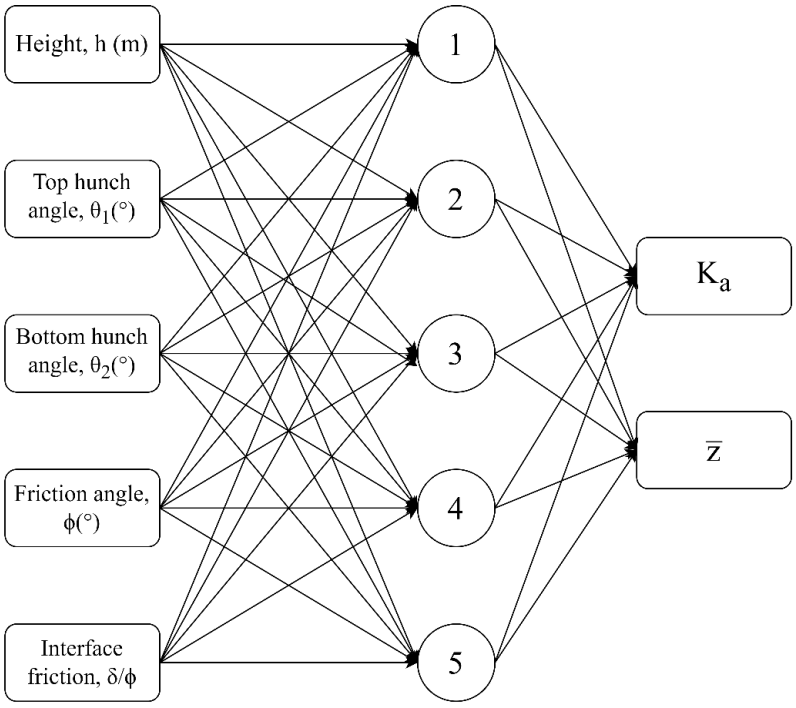

Fig. 4 Network diagram for the present study

$$\tanh(x) = \frac{2}{1 + e^{-2x}} \tag{9}$$

$$\text{Output} = \sum_{i=1}^{N_h} W^{2,i} \tanh\left(\sum_{j=1}^{J} W^{1,i} x^j + b_a{}^{1,i}\right) + b_a{}^{2,i} \tag{10}$$

Optimizing the performance of the training ANN model involves monitoring error parameters such as root mean squared error (RMSE), mean absolute percentage error (MAPE), coefficient of determination (R^2), and scatter index (SI). A lower magnitude of error parameters (RMSE, MAPE, SI) and a higher R^2 signify a superior fit. The performance of these error parameters for the training ANN model is presented in Fig. 3. It can be noticed that beyond 5 nodes in the hidden layer, most error parameters approach a constant, satisfactory value for both the output parameters. Hence, the hidden layer is designed with 5 nodes for the present network. Consequently, a network with an architecture of 5-5-2, as shown in Fig. 4, was finalized to assess the performance of various training functions and undergo further analysis.

3.4.3 Performance of Training Functions

In the training of models, the primarily assigned weights are combined with the likelihood of observed data to update the weights. It helps prevent overfitting by discouraging the

Table 3 Performance analysis of various training functions on the training dataset

Optimization function	R^2	RMSE	MAPE (%)	SI
Active earth pressure coefficient, K_a				
Levenberg-Marquardt	0.9403	0.0242	8.09	10.64
Bayesian Regularization	**0.9409**	**0.0241**	**7.69**	**10.58**
BFGS Quasi-Newton	0.9307	0.0261	9.49	11.46
Resilient Backpropagation	0.9036	0.0307	13.25	13.52
Scaled Conjugate Gradient	0.9353	0.0252	9.02	11.07
Conjugate Gradient with Powell/Beale Restarts	0.9336	0.0255	9.17	11.21
Fletcher-Powell Conjugate Gradient	0.9322	0.0258	9.31	11.34
Polak-Ribiére Conjugate Gradient	0.9346	0.0253	9.09	11.14
One Step Secant	0.8211	0.0419	17.84	18.41
Variable Learning Rate Gradient Descent	0.8989	0.0315	13.09	13.84
Point of application of earth pressure, $\bar{z}$				
Levenberg-Marquardt	0.8984	0.0163	1.35	4.20
Bayesian Regularization	**0.9252**	**0.0139**	**1.64**	**3.60**
BFGS Quasi-Newton	0.7812	0.0239	3.58	6.16
Resilient Backpropagation	0.7962	0.0231	3.82	5.94
Scaled Conjugate Gradient	0.8301	0.0211	2.97	5.43
Conjugate Gradient with Powell/Beale Restarts	0.8184	0.0218	3.21	5.61
Fletcher-Powell Conjugate Gradient	0.8282	0.0212	3.21	5.46
Polak-Ribiére Conjugate Gradient	0.8267	0.0213	3.19	5.48
One Step Secant	0.2477	0.0440	7.87	11.42
Variable Learning Rate Gradient Descent	0.5247	0.0353	6.03	9.08

development of overly intricate models and promoting solutions characterized by weight configurations that are more likely under the specified prior distribution (Goh *et al.* 2005, Feng and Jimenez 2015, Zhang *et al.* 2021, Kim *et al.* 2022, Nguyen *et al.* 2022).

Various algorithms are available for training Artificial Neural Network (ANN) models, including i) Levenberg-Marquardt (LM), ii) Stochastic Gradient Descent (SGD), iii) Bayesian Regularization, and others. It is imperative to evaluate the performance of different training algorithms to substantiate the choice of the training algorithm for this study. The performance of 10 such algorithms was assessed for the selected neural architecture by comparing their error parameters, as mentioned earlier. The relevant comparison is presented in Table 3, revealing that the Bayesian Regularization (BR) algorithm stands out as the most efficient.

It exhibits the lowest Root Mean Squared Error (RMSE), Mean Absolute Percentage Error (MAPE), and Scatter Index (SI) values, along with the highest R^2 values of 0.940 and 0.925 for outputs K_a and $\bar{z}$, respectively. The Variable Learning Rate Gradient Descent algorithm demonstrated inferior performance among the various algorithms considered, as indicated by the error parameter values in Table 3. Consequently, the Bayesian Regularization algorithm is used to develop the model and predictions further. Note that Bayesian regularization, also known as weight decay regularization, introduces a prior distribution of the network weights, treating them as random variables rather than fixed parameters.

4. Development of analytical solution

In addition to a robust ANN model, an approximate analytical solution for a hunch back wall with unsaturated backfill has been proposed, adhering to the assumptions by Coulomb (1776). Fig. 5 shows an overall schematic for calculating earth pressures as well as suction stresses. Note that the active earth pressure coefficient for dry backfill can be calculated using Coulomb's expression

$$K_{ac} = \frac{\cos^2(\phi' - \theta)}{\cos^2\theta\cos(\theta+\delta)\left[1+\left\{\frac{\sin(\phi'+\delta)\sin\phi'}{\cos(\theta-\delta)\cos\theta}\right\}^{1/2}\right]^2} \quad (11)$$

Referring to Fig. 5, the active thrust along the top portion of the wall, P_{a1}, can be calculated as

$$P_{a1} = \frac{1}{2}K_{ac1}\gamma h_1^2 \quad (12)$$

Similarly, following the pressure diagram and subsequent simplification, the active thrust along the bottom portion of the wall, P_{a2}, can be calculated as

$$P_{a2} = \frac{1}{2}h_2 K_{ac2}\gamma(h_1 + h) \quad (13)$$

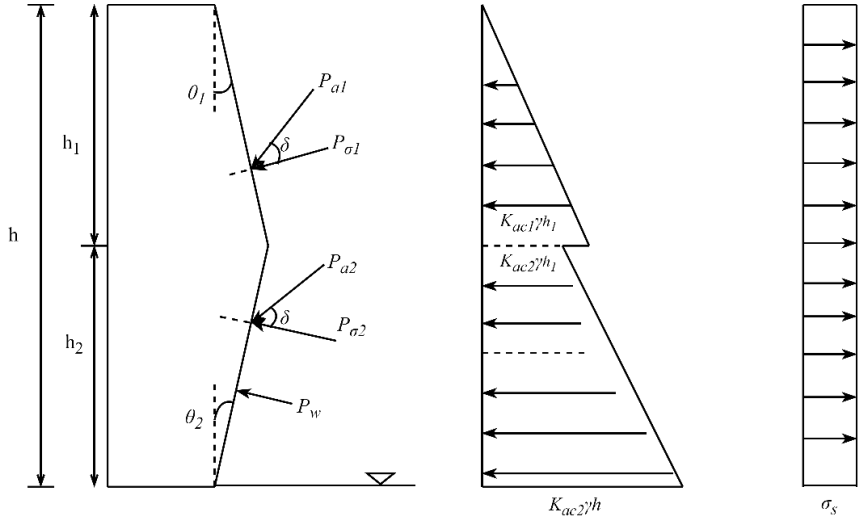

Fig. 5 Schematics for development of analytical solution

In expressions 12 and 13, K_{ac1} and K_{ac2} represent active earth pressure coefficients corresponding to the top and bottom portion of the wall inclined at $\theta_1°$ and $\theta_2°$, respectively.

In order to incorporate the effect of suction stress into the analytical model, an expression was developed by considering the weighted average of σ_{pw} values (obtained as per Eq. (4)) along the depth of the wall and termed as σ_s . In this regard, the suction stress profile shown in Fig. 2, was assessed for heights ranging from 4m to 10m. These average suction stresses (σ_s) were plotted against the respective wall heights to establish a simple regression equation

$$\sigma_s = 0.2292h - 3.6603 \tag{14}$$

Using the above expression, the suction force $P_{\sigma s1}$ and $P_{\sigma s2}$ above and below the hunch position can be estimated as

$$P_{\sigma s1} = \sigma_s \frac{h_1}{\cos\theta_1}\ , P_{\sigma s1} = \sigma_s \frac{h_2}{\cos\theta_2} \tag{15}$$

Following above, the horizontal and vertical components of active thrust on the retaining wall with the consideration of suction force can be determined as

$$P_h = P_{a1}\cos(\theta_1 + \delta) + P_{a2}\cos(\delta - \theta_2) - P_{\sigma s1h} - P_{\sigma s2h} \tag{16}$$

$$P_v = P_{a1}\sin(\theta_1 + \delta) + P_{a2}\sin(\delta - \theta_2) - P_{\sigma s1v} - P_{\sigma s2v} \tag{17}$$

Where $P_{\sigma s1h}$, $P_{\sigma s2h}$ and $P_{\sigma s1v}$, $P_{\sigma s2v}$ are the horizontal and vertical components of suction force acting on the wall. Total active thrust (P_a) is calculated as the resultant of P_h and P_v, while the active earth pressure coefficient for a hunched wall can be determined using Eq. (8), mentioned earlier.

5. Results and discussions

The study investigates the effect of various parameters, including wall height (h) at 4m, 6m, 8m, and 10m; top and bottom hunch angles (θ_1, θ_2) between 0°- 20° corresponding to various hunch positions detailed in Table 1; internal friction angle of soil (ϕ) ranging from 20° to 45°; and wall interface friction angle (δ) at 0, $\phi/3$, $\phi/2$, $2\phi/3$, and ϕ on the lateral earth pressure. The position of the water table is considered at the toe of the wall. The observations from this study are summarized in the subsequent paragraphs.

5.1 Variation of active earth pressure coefficient, K_a

The changes in K_a values for different combinations of θ_1 and θ_2 for ϕ=20°, 25°, 30°, 35°, 40° and 45° with δ/ϕ=0.5 for a wall height of 6m are displayed in Fig. 6. For the sake of clarity, various hunch positions are shown in Fig. 6(a). The colours deep blue and dark red in this figure, respectively, stand for the lowest and highest values of K_a. Upon analyzing these figures closely, it becomes evident that increasing the hunch angle decreases K_a gradually for a specific hunch position. When θ_1 or θ_2 approach 20°, the most significant reduction in K_a is observed. For instance, with the hunch positioned at one-third of the wall height from the top (h_1/h=1/3 or h_1/h_2 =1/2), the decrease in K_a due to a change in the hunch angle from $\theta_1=\theta_2=0°$ to θ_1=20°, θ_2=10.3° is approximately 15% across all ϕ values.

Likewise, when the hunch is placed at mid-height (h_1/h=1/2 or h_1/h_2 =1), the decrease in K_a from a vertical wall (θ_1 = θ_2 = 0) to a hunchback wall (θ_1 = θ_2 = 20°) is 17% for ϕ=20° and 19% for ϕ=45°. The reduction in K_a values was significant for rough walls and greater friction angles. This pattern becomes more pronounced as the hunch position moves towards the bottom of the wall (h_1/h=2/3 or h_1/h_2 =2). The reduction in K_a due to a change in the hunch angle from $\theta_1=\theta_2=0°$ to θ_1=10.3°, θ_2=20° is 25% for ϕ=20°, while it is 60% for ϕ=45°. In summary, it can be concluded that placing the hunch at 2h/3 distance from the top of the wall is most effective with a hunch angle of θ_2=20°.

It is essential to highlight that the lower portion of the wall is primarily affected by the unsaturation effect. Therefore, a significant decrease in the K_a value with hunch inclusion near the lower portion of the wall is justified.

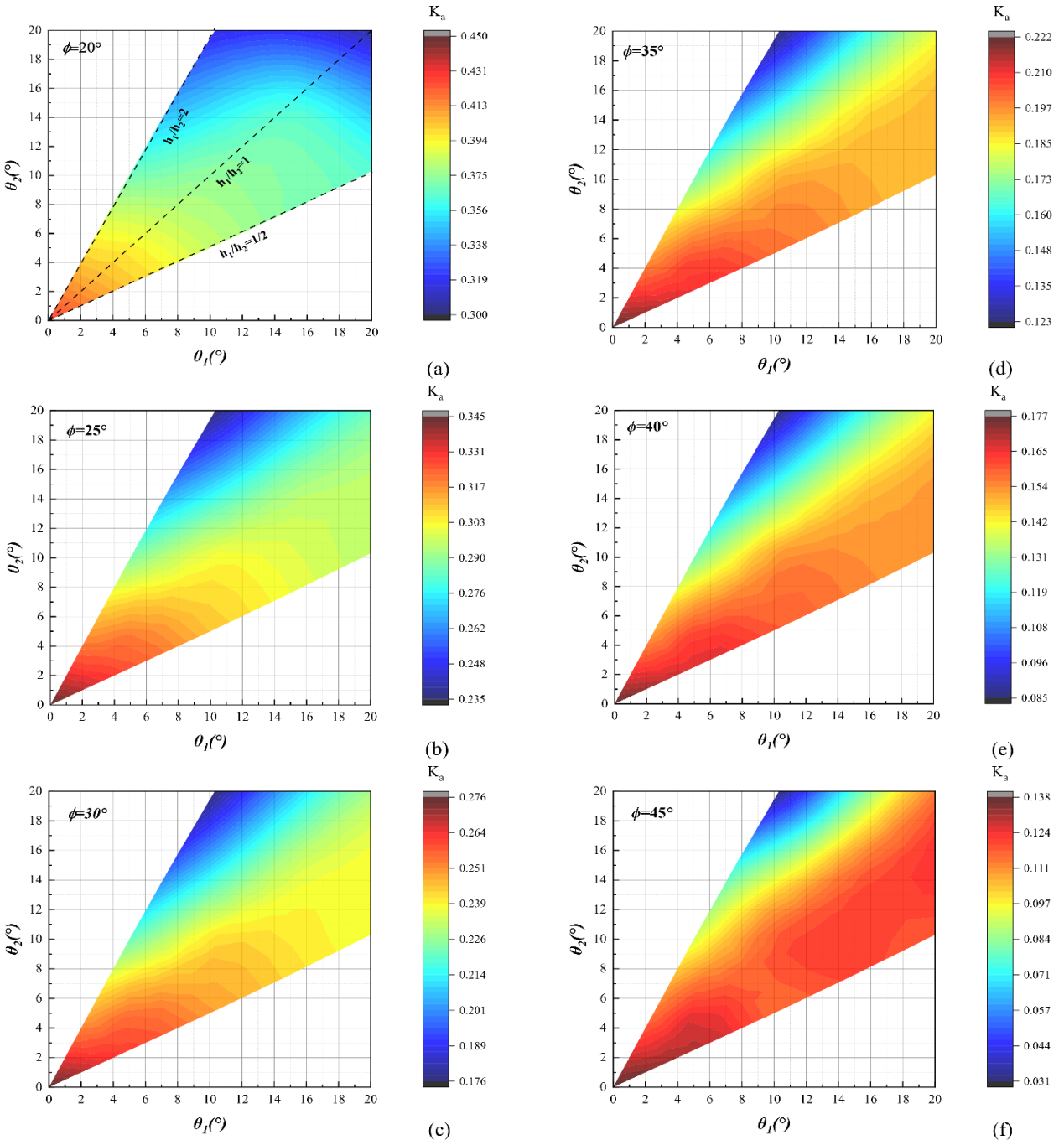

Fig. 6 Variation in K_a with hunch angles

5.2 Effect of wall height on K_a

As previously stated, the influence of unsaturation on active earth pressure diminishes as the height of the wall increases. Consequently, it was decided to examine this impact for a vertical as well as hunch back wall spanning from 4 meters to 10 meters in height. The friction angle of the backfill soil (ϕ) was taken as 30° and 40°, while the wall roughness (δ/ϕ) was assumed to be 0, indicating a smooth wall surface.

With these considerations, the variation in active earth pressure coefficient K_a with wall height is shown in Fig. 7(a) for vertical wall and Fig. 7(b) for wall with hunch at mid-height.

The K_a values corresponding to dry soil conditions, i.e., without considering unsaturation, are also depicted in these figures to facilitate comparison. Note that in Fig. 7(b), the K_a values for the hunch back wall (h_1/h_2=1) with dry backfill were taken from Thottoth *et al.* (2024b). Upon examining Fig. 7, it can be noted that the K_a value rises as the wall height increases, gradually approaching that of dry soil. It implies that the effect of unsaturation diminishes as the wall height increases. Moreover, the difference in the K_a value between dry and unsaturated backfill is particularly pronounced for shorter walls, i.e., h= 4 m

It is pertinent to mention that with selected values of material parameters (α_a and n_p in Eq (4)), the zone of

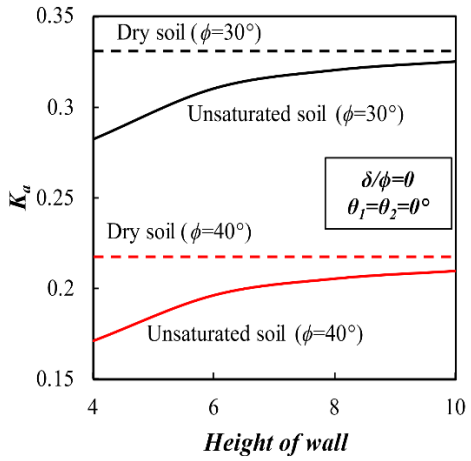

(a) Vertical wall

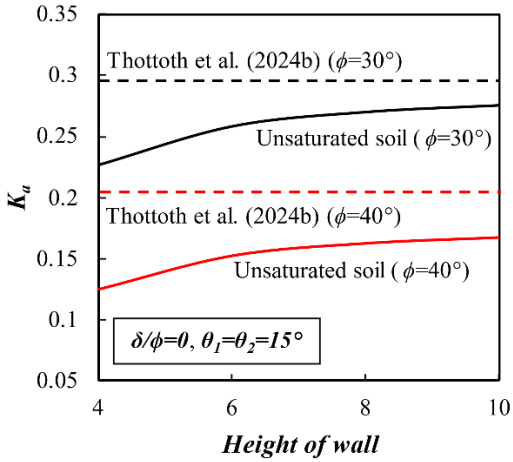

(b) Hunchback wall (h_1/h =1/2)

Fig. 7 Effect of wall height on K_a

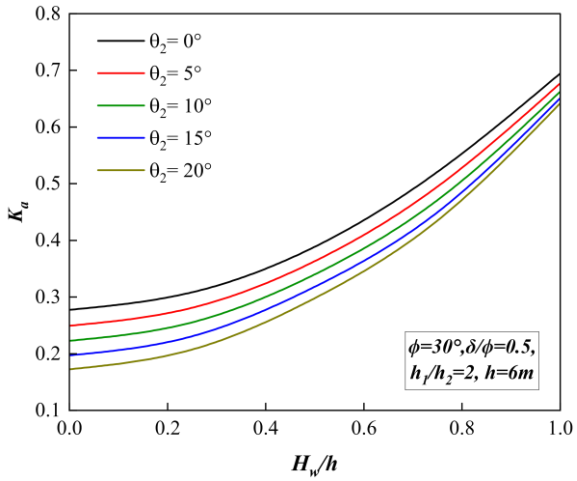

Fig. 8 Variation of K_a with change in water table position

unsaturation in the present case extends up to approximately 2m - 3m above the toe of the wall. Consequently, the unsaturation effect is perceived over a larger portion of the failure wedge for shorter walls, leading to a lower K_a value. Conversely, as wall height increases, the influence of unsaturation in relation to the wall height reduces, resulting in a higher K_a value.

5.3 Effect of water table position on K_a

It is important to note that retaining walls are primarily designed to withstand earth pressure rather than water pressure, although temporary increases in water table levels due to rainfall or other natural factors can occur. While this study primarily examines the unsaturation effect by considering the water table at the toe of the wall, a parametric study has also been conducted by varying the water table position along the wall height. For this analysis, a hunchback wall with h_1/h_2=2 was used, with backfill properties set at, ϕ=30°, δ=ϕ/2 and wall height, h=6 m. The water table position was varied from the toe of the wall to ground level (with H_w/h ranging from 0 to 1).

Fig. 8 illustrates the variation of the active earth pressure coefficient K_a as the water table position changes. The figure shows that the active earth pressure coefficient may increase to 4 times for vertical as well as hunch back walls, as H_w/h changes from 0 to 1. This observation aligns with the findings reported by Fathipour *et al.* (2020), for a vertical wall. Notably, the K_a values for hunchback retaining walls are slightly lower than those for vertical walls across different water table positions, supporting the use of hunchback walls even when a water table is present.

5.4 Effect of soil-wall interface friction (δ/ϕ) on K_a

This study conducted a comprehensive parametric analysis to examine the impact of soil-wall interface friction (δ/ϕ) on the active earth pressure coefficient. However, the K_a values presented in Fig. 6 were shown for δ/ϕ = 0.5 for clarity. The variation of K_a is further detailed here for a range of δ/ϕ values between 0-1. The analysis considered a wall height of 6m with h_1/h_2=1/2, 1, 2 and soil friction angles of ϕ=30° and 40°. The resulting variation of K_a is summarized in Table 4.

As expected, the results in Table 4 indicate that K_a decreases as δ/ϕ increases for all geometries and friction angle values. However, the reduction in K_a when δ/ϕ changes from 0 to 1 is only about 10% to 15% across all cases, which is relatively minor.

5.5 Effect of $1/\alpha_a$ and n_p on K_a

This part of the study examines the impact of unsaturation parameters, specifically air entry pressure ($1/\alpha_a$) and pore size number (n_p), on the active earth pressure coefficient. It is important to note that flow conditions do not influence suction stress estimation in sand, so these parameters were not included in the investigation. The study focuses on cohesionless soils, with selected ranges of $1/\alpha_a$ and n_p representing soil types such as silt and sand. The α_a values were chosen as 0.1 kPa^{-1}, 0.01 kPa^{-1} and 0.001 kPa^{-1}, while the n_p values were set at 2, 5, and 8.5. These ranges are consistent

Table 4 Variation of K_a values with respect to δ/ϕ for hunchback wall

Geometry	θ	ϕ=30°					ϕ=40°				
		δ=0	*δ=ϕ/3*	*δ=ϕ/2*	*δ=2ϕ/3*	*δ=ϕ*	*δ=0*	*δ=ϕ/3*	*δ=ϕ/2*	*δ=2ϕ/3*	*δ=ϕ*
Vertical wall	**0**	0.3102	0.2839	0.2759	0.2690	0.2651	0.1965	0.1799	0.1762	0.1757	0.1749
h_1/h_2 = 1/2	**5**	0.2987	0.2723	0.2641	0.2566	0.2543	0.1858	0.1702	0.1653	0.1641	0.1625
	10	0.2851	0.2609	0.2525	0.2447	0.2418	0.1754	0.1589	0.1556	0.1531	0.1525
	15	0.2757	0.2493	0.2410	0.2330	0.2296	0.1651	0.1490	0.1450	0.1431	0.1424
	20	0.2636	0.2375	0.2292	0.2211	0.2176	0.1546	0.1391	0.1353	0.1333	0.1325
h_1/h_2 = 1	**5**	0.2859	0.2664	0.2582	0.2511	0.2480	0.1806	0.1641	0.1602	0.1588	0.1545
	10	0.2744	0.2496	0.2414	0.2336	0.2306	0.1657	0.1500	0.1462	0.1447	0.1439
	15	0.2582	0.2331	0.2252	0.2179	0.2151	0.1521	0.1378	0.1345	0.1334	0.1325
	20	0.2409	0.2174	0.2102	0.2038	0.2021	0.1405	0.1282	0.1259	0.1266	0.1228
h_1/h_2 = 2	**5**	0.2898	0.2605	0.2486	0.2381	0.2292	0.1757	0.1551	0.1486	0.1418	0.1386
	10	0.2580	0.2313	0.2226	0.2137	0.2090	0.1480	0.1318	0.1273	0.1241	0.1244
	15	0.2327	0.2063	0.1974	0.1879	0.1821	0.1252	0.1097	0.1051	0.1010	0.0997
	20	0.2075	0.1816	0.1727	0.1628	0.1563	0.1031	0.0885	0.0839	0.0793	0.0767

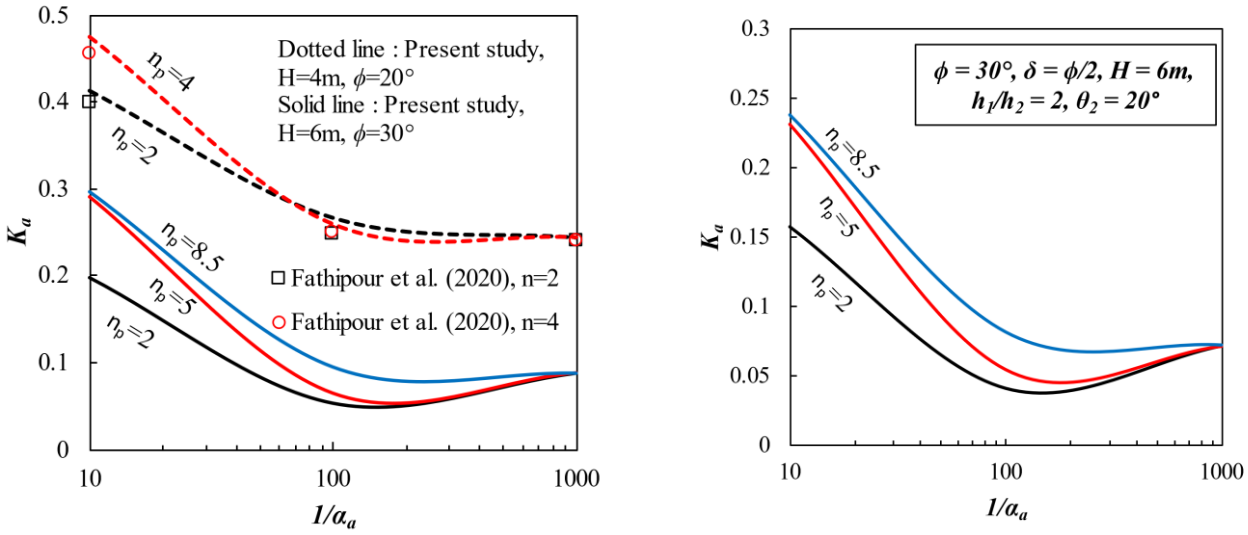

(a) (b)

Fig. 9 Effect of unsaturation parameters on K_a

with those used in studies by Fathipour *et al.* (2020) and Vahedifard *et al.* (2015a).

The analysis was conducted for both a vertical wall (H=4m, 6m, ϕ =20º, 30º) and a hunched wall (h_1/h_2 =2, θ=20º, H=6m, ϕ =30º). Fig. 9 illustrates the relevant variation in the active earth pressure coefficient.

Fig. 9(a) also includes a comparison with results from Fathipour *et al.* (2020) for a vertical wall of 4 meters, showing a favorable agreement. Observations from Fig. 9 indicate that K_a values remain constant for any n_p values at a lower α_a (0.001 kPa^{-1}). Conversely, at higher α_a values, the K_a value increases with a rise in n_p. It implies that fine-grained soils are more affected by changes in air entry pressure than coarser soils like clean sand.

5.6 Effect of hunch back wall geometry on the point of application of active earth pressure

Note that studies are available on analyzing a hunch back wall in dry soil, but none address unsaturated backfill. Additionally, there is a gap in the literature concerning the point of application of resultant active thrust. This aspect was investigated in the current study. Consequently, an analysis was conducted with friction angle (ϕ) 25°, 35° and δ/ϕ = 0.5. The wall height (h) was considered 4m and 10m. Fig. 10 illustrates the variation in the point of application, represented as $\bar{z}/h$ (normalized with the wall height), with different back face geometries corresponding to hunch angles listed in Table 1. In Fig. 10, the hunch angle θ should correspond to θ_1 for h_1/h_2 =1/2, 1, and θ_2 for h_1/h_2 =2.

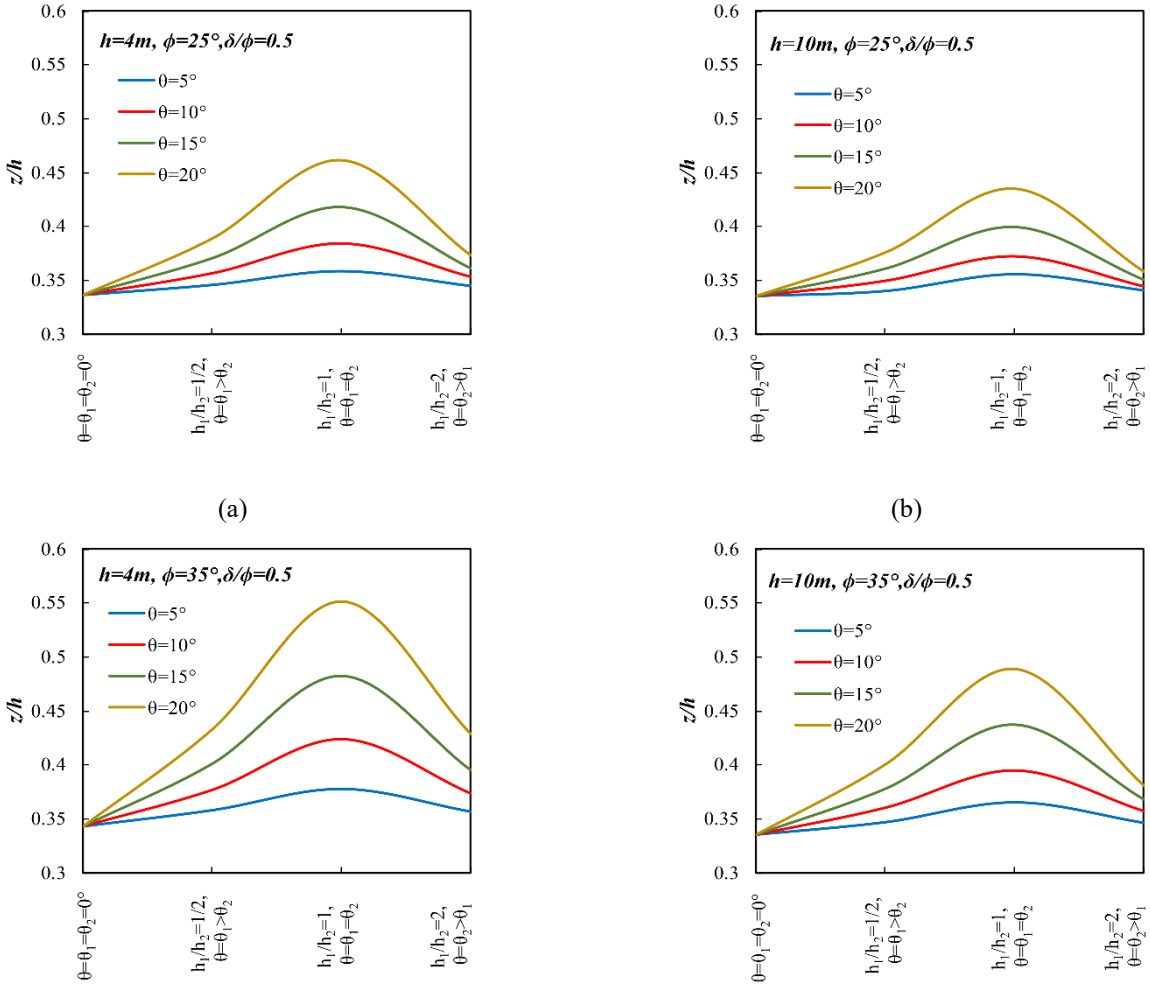

Fig. 10 Variation of point of application of active thrust with hunch back geometry

The graph clearly shows that introducing a hunch causes the point of application $\bar{z}$ to move upwards. Notably, $\bar{z}$ remains at 0.33 for a vertical wall, consistent with established theories. The maximum $\bar{z}$, is observed when the hunch angle is at its maximum, i.e., 20°. Transitioning the hunch position from h/3 to h/2 results in $\bar{z}$ varying from 0.4 to 0.46 for a 4 m wall with θ=20° and ϕ=25°, while the change in hunch position to 2h/3 (h_1/h_2=2) reduces $\bar{z}$ to 0.41. Moreover, $\bar{z}$ decreases with an increase in wall height, as evident in Fig. 10, where the maximum $\bar{z}$ of 0.46 for the 4 m wall drops to 0.42 for h=10 m. Additionally, increasing the friction angle causes the point of application to move upward relative to the toe of the wall.

Acknowledging that the hunchback configuration of the wall redistributes pressure, lowering it at the bottom of the wall while increasing it along the top, resulting in an overall reduction in active earth pressure. Additionally, it was observed that as the friction angle rises and the wall height decreases, the ratio of active thrust corresponding to the top and bottom sections increases. Consequently, the point of application of total active thrust moves upward in such cases, justifying the reported behavior.

5.7 Stability analysis

For a more thorough analysis of the hunchback retaining wall, the factors of safety concerning sliding and overturning were determined. The stability assessments were carried out for vertical and hunch walls by considering equal areas for a rational comparison. The computations were performed for a wall height of 6 m with ϕ=35°, δ/ϕ = 0.5. Initially, a vertical wall measuring 6 m in height with a base width of 0.3h was considered. Subsequent hunchback wall configurations were obtained by maintaining an area equal to the vertical wall and adjusting the base width while keeping the hunch angles consistent with Table 1. With this consideration, the variations in the sliding factor of safety ($FOS_{sliding}$) and overturning factor of safety ($FOS_{overturning}$) for different hunch positions are depicted in Fig. 11. In these figures, the notation θ refers to θ_1 for wall with hunch at h/3 and h/2 while it is considered θ_2 for hunch at 2h/3.

An observation of Fig. 11 indicates that both safety factors increase as the hunch angle θ rises from 0° to 20° for all geometries. The hunchback wall with h_1/h=2/3, θ_1=10.3°, and θ_2=20° exhibits the most substantial enhancement in safety

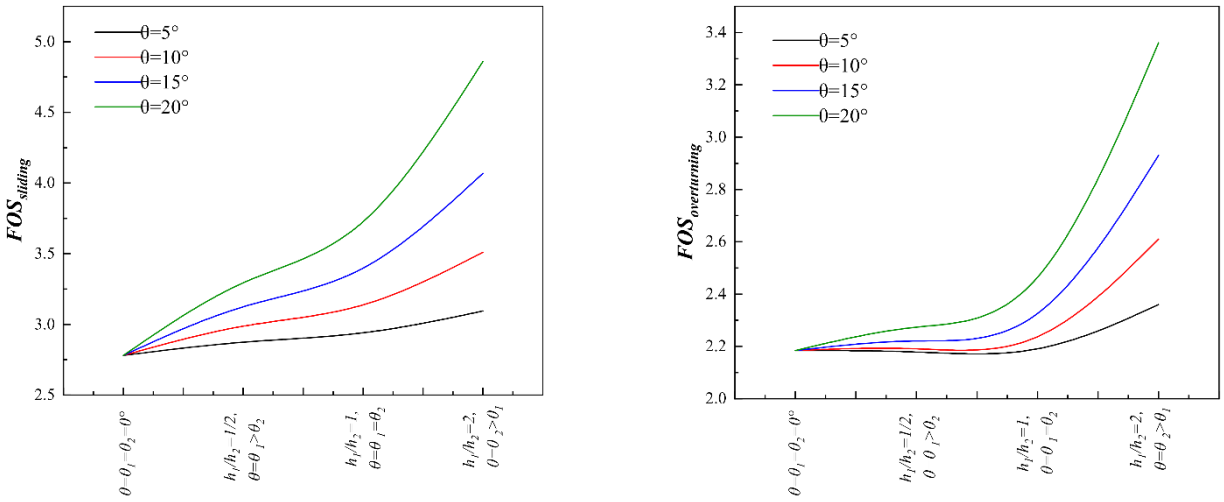

(a) Sliding factor of safety, $FOS_{sliding}$ (b) Overturning factor of safety, $FOS_{overturning}$

Fig. 11 Variation of the Factor of safeties for hunch back wall with unsaturated backfill.

factors compared to a vertical wall (with $\theta_1 = \theta_2 = 0°$), amounting to 1.8 times for $FOS_{sliding}$ and 1.6 times for $FOS_{overturning}$. These findings further support the implementation of hunchback retaining walls.

5.8 Active earth pressure distribution

This analysis investigates the earth pressure distribution behind both vertical and hunched retaining walls, considering suction stresses and hunch provision. Fig. 12(a) illustrates the relevant active earth pressure distribution for the vertical wall and compares it with the findings of Fathipour *et al.* (2020) based on lower bound limit analysis and Lu and Likos (2004) limit equilibrium solution. This comparison indicates that the current pressure distribution, utilizing horizontal slice methodology, is consistent with the rigorous approach employed by Fathipour *et al.* (2020). Additionally, it slightly outperforms the existing limit equilibrium solution by Lu and Likos (2004), utilizing a linear failure wedge.

Building on this insightful comparison, the impact of hunch position on earth pressure distribution is explored for a retaining wall with $\phi = 35°$ and $\delta/\phi = 0.5$. The variation of active earth pressure distribution for hunch positions at $h_1/h_2 = 1/2$, 1, and 2 is depicted in Figs. 12(b)-12(d), respectively. Observations from these figures reveal nonlinear variations in active earth pressure within the zone approximately 1 m-2 m above the toe of the wall (z/h = 0.8-0.9). This behavior is attributed to a notable peak in the suction stress profile presented in Fig. 2. Additionally, the discontinuity in pressure distribution results from including a hunched section.

In conclusion, it can be summarized that including a hunch leads to an increase in pressure above the hunch and a decrease below it, thus leading to an overall reduction of earth pressure. The presence of suction stresses further contributes to a reduction in active earth pressure. Consequently, an analysis of hunched walls considering the unsaturation effect is justified.

5.9 Failure patterns

Figs. 13(a)-13(c) visually depict the failure surfaces associated with hunchback walls, corresponding to $\phi = 35°$ and $\delta = 0.5\phi$, representing three distinct hunch positions explored in the study. Analysis of these figures reveals that introducing a hunch results in a bilinear failure surface, consistent with the pressure distribution previously presented (Figs. 12(b) and 12(d)), which demonstrates a discontinuity in pressure at the hunch position due to the change in the back-face inclination of the wall.

Further scrutiny of these figures indicates a reduction in the area of the failure wedge with an increase in the hunch angle for all three geometries. For the first case, i.e., h_1/h_2=1/2, when θ_1 changes from 5° to 15°, there is a reduction of approximately 13% in the failure wedge area. Similarly, when h_1/h_2=1 and 2, this reduction amounts to 16% and 20%, respectively. This observation justifies the reduction in active earth pressure with an increase in hunch angle.

A further examination of Fig. 13 suggests that suction stress has minimal effect on the critical failure surface compared to its influence on the pressure distribution.

6. ANN performance measures

Assessing the accuracy of active earth pressure coefficient predictions in hunchbacked retaining walls supporting unsaturated soil under various soil and geometric conditions is essential. Table 5 provides performance measures for the current Artificial Neural Network (ANN) model across training, testing, and overall datasets. Figs. 14(a)-14(c) depict these data sets' predicted and targeted K_a and $\bar{z}$ values, showcasing a significant portion of data closely aligning with the center-line, indicating optimal model performance.

More specifically, the model's performance is evaluated using several metrics, including Mean Squared Error (MSE), Root Mean Squared Error (RMSE), Mean Absolute Percentage Error (MAPE), Scatter Index (SI), and Coefficient of Determination (R^2). The formulas for calculating these metrics can be found in literature sources (Gnananandarao *et al.* 2020; Amjad Raja *et al.* 2023) and are not reiterated here. A perfect fit is indicated when MSE and RMSE approach 0 while R^2

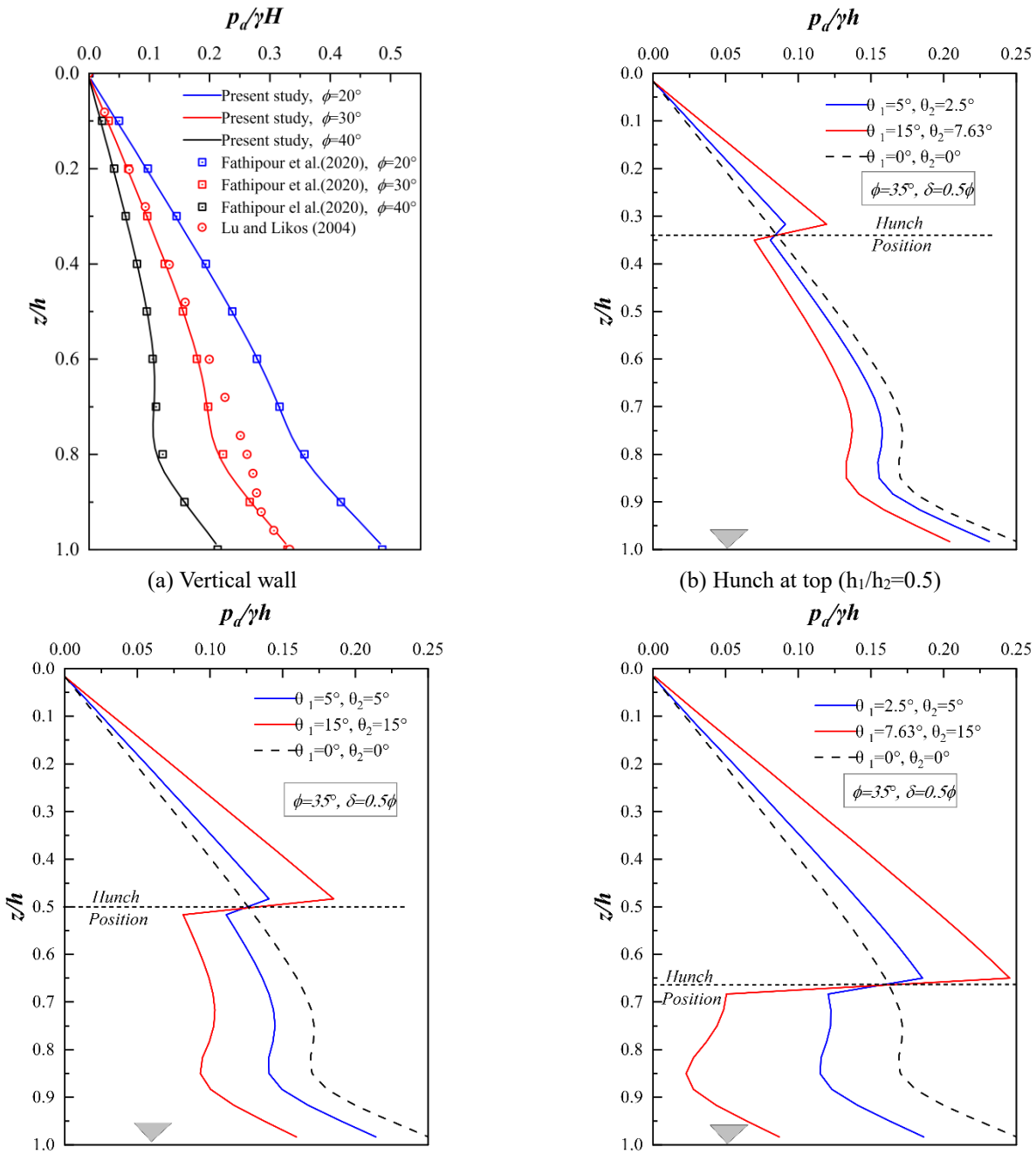

(a) Vertical wall

(b) Hunch at top (h_1/h_2=0.5)

(c) Hunch at middle (h_1/h_2=1)

(d) Hunch at bottom (h_1/h_2=2)

Fig. 12 Active earth pressure distribution for vertical and hunchback walls

Table 5 Error parameters for the developed ANN model

	R^2	MSE	RMSE	MAPE	SI
		Output 1, K_a			
Training	0.941	0.0005	0.0241	7.691	10.571
Testing	0.947	0.0005	0.0232	7.898	9.872
Overall	0.942	0.0005	0.0238	7.732	10.434
		Output 2, $\bar{z}$			
Training	0.925	0.0002	0.0139	1.639	3.602
Testing	0.934	0.0001	0.0113	1.568	2.953
Overall	0.926	0.0002	0.0135	1.625	3.484

approaches 1. Table 5 reveals that MSE and RMSE values were close to zero for all three datasets. The coefficient of determination (R^2) is estimated at 0.94 for output K_a and 0.93 for output $\bar{z}$, together with a MAPE value of less than 10%, indicating an excellent fit. Furthermore, a lower SI value, representing the percentage of expected error, is desirable.

In conclusion, all error parameters, as shown in Table 5, fall within an acceptable range, indicating a very good fit of the model for both outputs across training, testing, and overall datasets. Therefore, it can be concluded that the developed ANN model predicts K_a and $\bar{z}$ with reasonable accuracy.

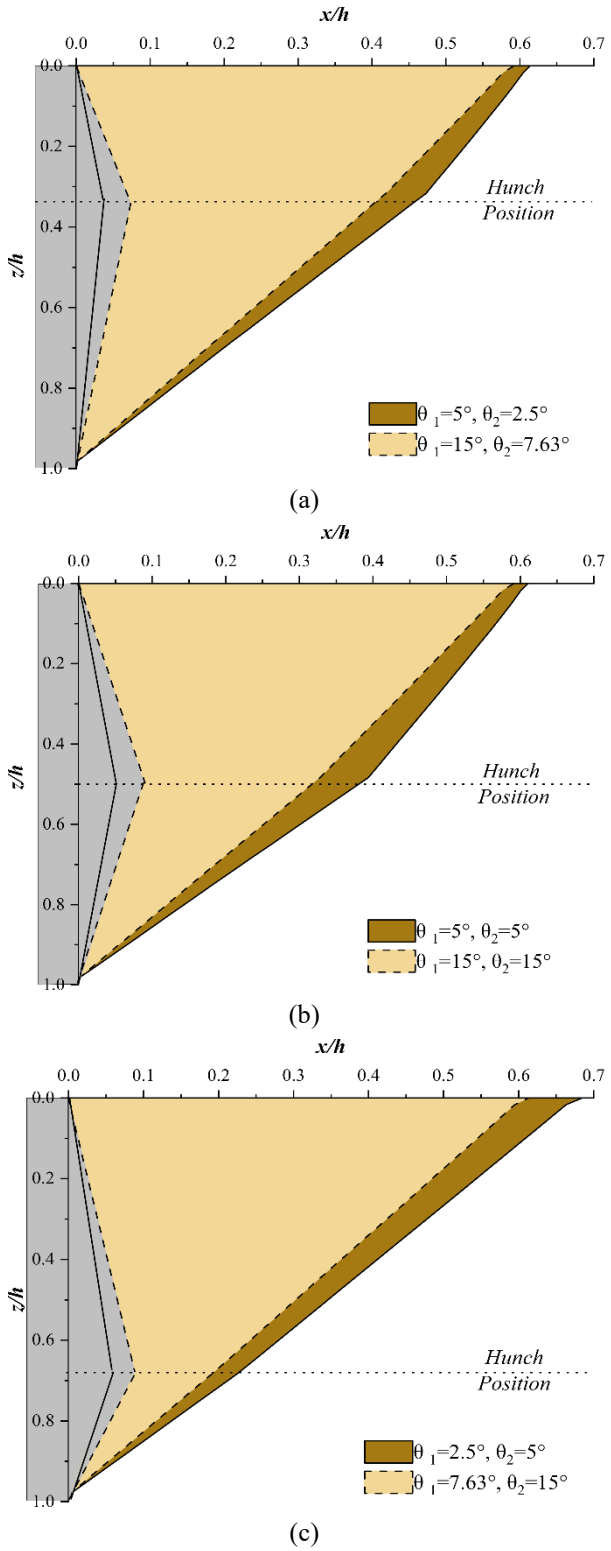

Fig. 13 Failure surface for different hunch positions

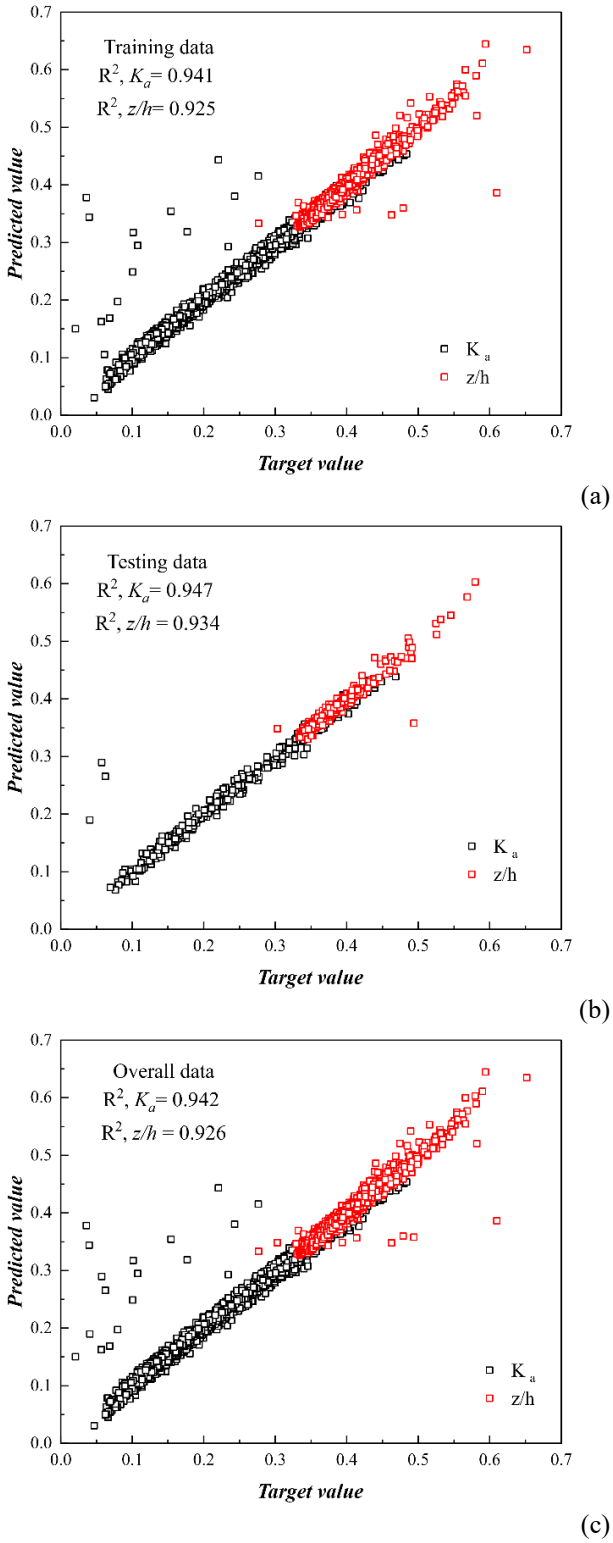

Fig. 14 Comparison of predicted versus actual data for (a) training, (b) testing and (c) overall datasets

7. ANN expression

Utilizing the outcomes from the developed ANN network, an expression can be formulated to calculate the active earth pressure coefficient and point of application of active thrust. The associated weights and biases obtained from the network to achieve this are presented in Table 6. As mentioned earlier, the hyperbolic tangent function is employed for the hidden layers, and the linear transfer function is used for the output layer in this study. The general expression for this calculation is already mentioned earlier.

Using the weights and biases obtained from the developed ANN model, expressions for output K_a and $\bar{z}$ can be written as

Table 6 Weights and Biases matrix for developed ANN model

Weights								Biases	
Hidden neurons	h	θ_1	θ_2	ϕ	δ/ϕ	K_a (Output 1)	$\bar{z}$ (Output 2)	Hidden layer	Output layer
1	-0.186	0.271	0.002	-0.115	-0.112	-0.087	3.123	-1.001	
2	0.176	-0.379	0.039	-0.874	0.053	0.523	1.256	0.713	Output 1 = 0.6734 Output 2 = 0.6599
3	0.182	0.027	-0.092	0.938	0.200	1.585	0.003	-0.979	
4	0.390	-0.523	-0.621	0.315	0.346	-0.579	-0.747	-1.310	
5	0.167	-0.306	-0.125	0.183	0.465	0.693	0.424	-1.018	

follows

$$K_a = -0.087C1 + 0.523C2 + 1.585C3 - 0.579C4 + 0.693C5 + 0.6734 \quad (18)$$

$$\bar{z} = 3.123C1 + 1.256C2 + 0.003C3 - 0.747C4 + 0.424C5 + 0.6599 \quad (19)$$

Where

$$C1 = \tan sig\,(-0.186\,h + 0.271\,\theta_1 + 0.002\,\theta_2 - 0.115\,\varphi - 0.112\,\delta/\varphi - 1.001) \quad (20)$$

$$C2 = \tan sig\,(0.176\,h - 0.379\,\theta_1 + 0.039\,\theta_2 - 0.874\,\varphi + 0.053\,\delta/\varphi + 0.713) \quad (21)$$

$$C3 = \tan sig\,(0.182\,h + 0.027\,\theta_1 - 0.092\,\theta_2 + 0.938\,\varphi + 0.200\,\delta/\varphi - 0.979) \quad (22)$$

$$C4 = \tan sig\,(0.390\,h - 0.523\,\theta_1 - 0.621\,\theta_2 + 0.315\,\varphi + 0.346\,\delta/\varphi - 1.310) \quad (23)$$

$$C5 = \tan sig\,(0.167\,h - 0.306\,\theta_1 - 0.125\,\theta_2 + 0.183\,\varphi + 0.465\,\delta/\varphi - 1.018) \quad (24)$$

Eqs. (18) and (19) can be used to predict K_a and $\bar{z}$ for a hunchback wall with unsaturated backfill, crucial parameters for stability analysis of the retaining wall. Hence, the developed model offers a practical and simplified solution for the implementation of hunchback walls.

8. Performance of analytical solution

Active thrust (P_a) obtained using the approximate analytical method described earlier is compared with the same from the numerical model as well as ANN predictions (Fig. 15).

It can be seen that both analytical solutions and ANN predictions show an appreciable fit with the numerical solutions. The analytical solution has an R^2 of 0.9458 with

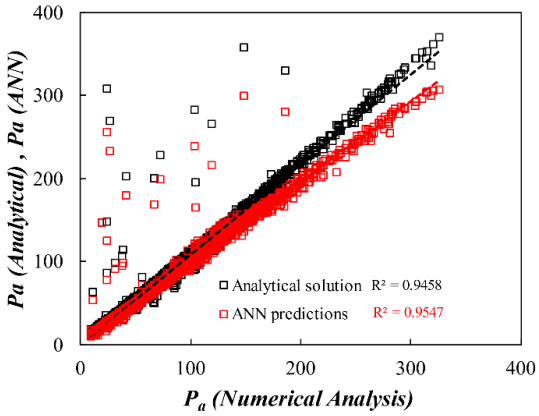

Fig. 15 Comparison of active thrust (P_a) obtained using ANN and analytical approach with numerical solution

an average deviation of 12.64%, while the ANN model outperformed the same with an R^2 of 0.9547 and an average deviation of 7.73%. It implies that the ANN prediction model is most suitable for accurately determining the active earth pressure in case of a hunched wall. However, one can follow the analytical approach for an approximate estimation of earth pressure.

In addition to the above, the variation in K_a with wall height and hunch angles computed using an analytical approach was compared with numerical solutions and displayed in Figs. 16(a) and 16(b)..

As expected, a noticeable difference is observed between numerical and analytical solutions, especially at lower wall height (Fig. 16(a)); irrespective of the wall geometry, a 5-10% difference in K_a is noted concerning numerical solution at h =4 m. However, at h=10 m, the analytical solution matches well with the numerical solution. It should be noted that suction stress has a significant effect on retaining walls with lesser height, while an increase in wall height diminishes the suction effect. Thus, the difference in suction stress calculation can be accounted for as the reason for the differences in K_a. When comparing the analytical solution to the numerical solution across different wall geometries and varying hunch angles, it is consistently observed that the analytical solution yields a lower value than the numerical one (Fig. 16(b)). Furthermore, the difference between both solutions remains fairly constant (3-10%) as the hunch angle ranges from 0° to 20°.

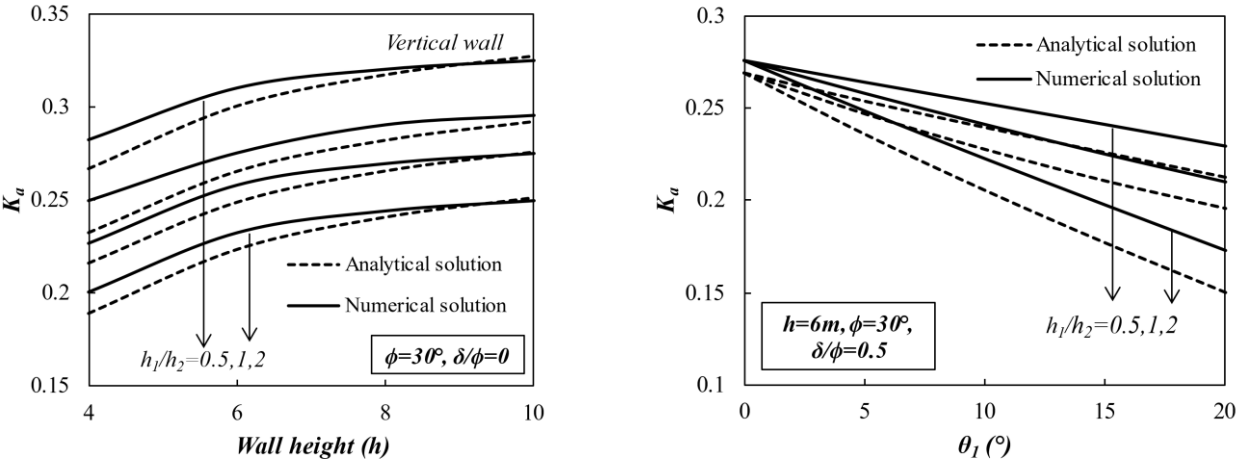

(a) (b)

Fig. 16 Variation in K_a with wall height and hunch angles obtained using analytical and numerical solutions

9. Comparison

The effectiveness of the developed expression was assessed by comparing the K_a values obtained from the ANN model as well as the analytical model with those reported by Fathipour *et al.* (2020) for unsaturated backfill, as well as the solutions provided by Chen and Liu (1990) and Yang and Chen (2021) for dry soil. This comparison, illustrated in Fig. 17, reveals a close alignment between the ANN predictions and the values Fathipour *et al.* (2020) reported, with only a slight deviation observed at ϕ=20°. The analytical solution appears to be lower in all the cases.

The predicted K_a values, influenced by the unsaturation effect, were slightly lower than those for dry soil, as reported by Chen and Liu (1990) and Yang and Chen (2021), thus supporting the rationale behind this study. This observation strongly suggests that the current ANN model can satisfactorily predict active earth pressure coefficients.

An analytical solution for static and seismic active earth pressure for vertical and inclined walls due to unsaturated backfill was presented by Ganesh and Rajesh (2021). Hence, the K_a and $\bar{z}$ for vertical wall, predicted using ANN, were compared with those from the literature. Table 7 presents the relevant comparison. It can be observed that the predicted $\bar{z}$ values match closely with that of the literature, while K_a values differ by a margin of approximately 10%. This marginal variation can be attributed to the use of a linear failure wedge by Ganesh and Rajesh (2021) for analytical solutions.

As mentioned before, the analysis of active earth pressure for hunchback walls considering unsaturated backfill is not available in the literature. Consequently, the active thrust values from the present study obtained using the predicted K_a values employing the ANN model and analytical model were compared with Sadrekarimi's (2017) experimental studies on hunchback retaining walls with a hunch at mid-height supporting dry backfill. Note that soil and wall properties reported in the literature (Sadrekarimi 2017) are: h = 10m, δ = 0, ϕ' = 34°, γ = 18.7 kN/m³. The same has been adopted here. The relevant comparison is depicted in Fig. 18. The observation of this figure indicates that the current trend of F_h aligns with that documented previously (Sadrekarimi 2017). However, the current F_h values are marginally lower in comparison to the literature due to the capillary effect. This discrepancy substantiates the motivation and rationale behind conducting the present study.

Similar to prior observations, the analytical solution, while comparable to the ANN forecast, was found to plot below it.

Table 7 Comparison of K_a and $\bar{z}$ with literature

	h=2 m		h=4 m	
	Ganesh and Rajesh (2021)	Present ANN prediction	Ganesh and Rajesh (2021)	Present ANN prediction
Active earth pressure coefficient, Ka	0.330	0.332	0.340	0.337
Point of application of active earth pressure, $\bar{z}$	0.198	0.220	0.278	0.240

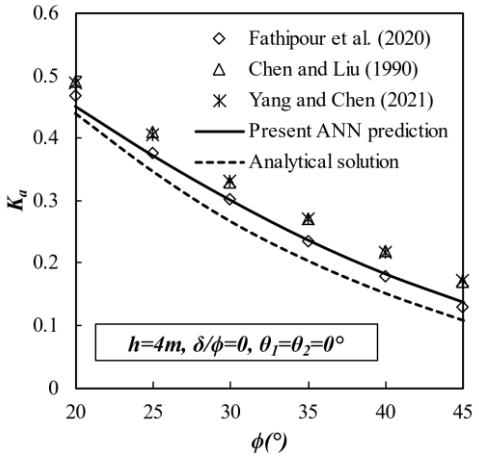

Fig. 17 Comparison of active earth pressure coefficient (K_a) obtained using ANN and analytical approach with the literature

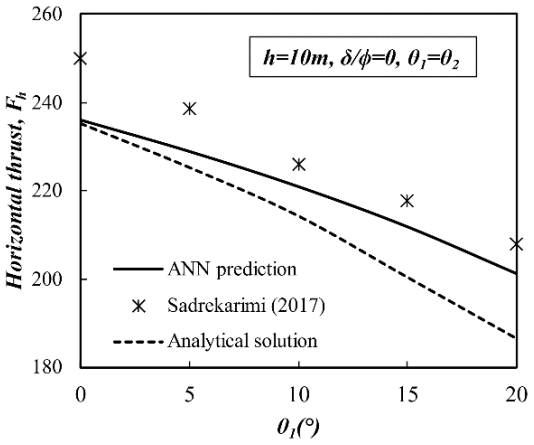

Fig. 18 Comparison of horizontal thrust calculated using ANN and analytical approach

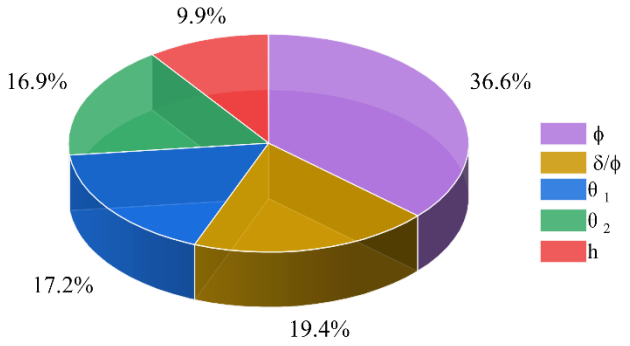

Fig. 19 Relative importance of input parameters

10. Sensitivity analysis

A sensitivity analysis was conducted to gain valuable insights into the primary factors influencing the active earth pressure coefficient in the context of a hunchback retaining wall with unsaturated backfill. The objective was to rank each variable according to its impact and eliminate input variables with minimal contributions to the proposed model. Researchers have suggested several methods for identifying crucial input parameters (Garson 1991, Olden and Jackson 2002). In this study, Garson's algorithm, which relies on weight configuration, was utilized to assess the contributions of the input variables.

The sensitivity analysis results depicted in Fig. 19 indicate that the internal friction angle (ϕ) influences the output most, accounting for 36.6% of the total impact, followed by the wall-soil interface friction (δ/ϕ) at 19.4%. The hunch angles (θ_1 and θ_2) affect the output by 17.2% and 16.9%, respectively.

On the other hand, the wall height (h) exhibits the least impact on the output, contributing only 9.9%. Notably, following the friction angle (ϕ), the combined influence of both hunch angles (θ_1 and θ_2) totals 34.1%, underscoring the justification for the current study. Despite the wall height having the least impact on the output, its significance should not be overlooked.

11. Conclusions

The study focuses on predicting the active earth pressure coefficient (K_a) and the point of application of pressure ($\bar{z}$) for a hunchback wall considering unsaturated backfill, incorporating input parameters such as wall heights, friction angles, hunch angles, and wall interface friction. Key findings include:

- Wall height emerges as one of the factors influencing earth pressure, leading to a maximum increase of 15% in active earth pressure coefficient with the increase in wall height from 4 m to 10 m. Additionally, the impact of suction stress diminishes with increasing wall height.
- Increasing hunch angles reduces the active earth pressure coefficient (K_a) for a given hunch position. Placing a hunch at a 2h/3 distance from the ground surface resulted in an optimal reduction in earth pressure in the 54-82% range, depending on the wall height.
- The examination of soil suction stress model parameters α_a and n_p indicates that the pore size parameter n_p affects K_a estimation at higher α_a values, which correspond to finer soils.
- The point of application of active thrust shifts upwards from the wall's toe with an increase in hunch angle. This shift is pronounced in wall geometries with a hunch at h/2 depth from the ground level, especially for backfills with higher friction angles.
- The developed active earth pressure was observed to be consistent with the literature, justifying the selected computational methodology.
- The presented analytical model estimates the active earth pressure values comparable to a numerical solution but slightly lower than ANN predictions.
- The developed ANN model exhibits excellent performance measures, with R^2 values of 0.94 and 0.93 for predicting K_a and $\bar{z}$, respectively. The predictions from the model were comparable with the literature and thus ensured the reliability of the present model in predicting the active earth pressure.
- Sensitivity analysis outcomes indicated that the earth pressure is most affected by the friction angle of soil and least by wall height. Moreover, the presence of hunch influenced the active earth pressure significantly, justifying the objective of the current study.

References

Abdollahi, M., Vahedifard, F., Abed, M. and Leshchinsky, B.A. (2021), "Effect of tension crack formation on active earth pressure encountered in unsaturated retaining wall bBackfills", *J. Geotech. Geoenviron. Eng.*, 147:. https://doi.org/10.1061/(ASCE)GT.1943-5606.0002434.

Acharyya, R., Dey, A. and Kumar, B. (2020), "Finite element and ANN-based prediction of bearing capacity of square footing resting on the crest of c-φ soil slope", *Int. J. Geotech. Eng.*, **14**, 176-187. https://doi.org/10.1080/19386362.2018.1435022.

Afsharpour, S., Payan, M., Chenari, R.J., Ahmadi, H. and Fathipour, H. (2022), "Bearing capacity of strip footings on

unsaturated soils under combined loading using LEM", *Geomech. Eng.*, **31**(2), 223-235. https://doi.org/10.12989/gae.2022.31.2.223.

Agarwal, E., Pain, A., Mukhopadhyay, T., Metya, S. and Sarkar, S. (2022), "Efficient computational system reliability analysis of reinforced soil-retaining structures under seismic conditions including the effect of simulated noise", *Eng. Comput.*, **38**, 901-923. https://doi.org/10.1007/s00366-020-01281-8.

Amjad Raja, M.N., Abbas Jaffar, S.T., Bardhan, A. and Shukla, S.K. (2023), "Predicting and validating the load-settlement behavior of large-scale geosynthetic-reinforced soil abutments using hybrid intelligent modeling", *J. Rock Mech. Geotech. Eng*., **15**, 773-788. https://doi.org/10.1016/j.jrmge.2022.04.012.

Aroni Hesari, S., Javankhoshdel, S., Payan, M. and Jamshidi Chenari, R (2022), "Pseudo-static internal stability analysis of geosynthetic-reinforced earth slopes using horizontal slices method", *Geomech. Geoeng.*, **17**, 1417-1442. https://doi.org/10.1080/17486025.2021.1940316.

Bahmani Tajani, S., Fathipour, H., Payan, M., Jamshidi Chenari, R. and Senetakis, K. (2023), "Temperature-dependent lateral earth pressures in partially saturated backfills", *Eur. J. Environ. Civ. Eng*., **27**, 3064-3090. https://doi.org/10.1080/19648189.2022.2125911.

Bardhan, A., Samui, P., Ghosh, K., Gandomi, A.H. and Bhattacharyya, S. (2021), "ELM-based adaptive neuro swarm intelligence techniques for predicting the California bearing ratio of soils in soaked conditions", *Appl Soft Comput*., **110**, 107595. https://doi.org/10.1016/j.asoc.2021.107595.

Bishop, A.W. (1959), "The principle of effective stress", *Tek Ukebl*, 859-863.

Chandaluri, V.K., Sawant, V.A. and Shukla, S.K. (2015), "Seismic stability analysis of reinforced soil wall using horizontal slice method", *Int. J. Geosynth. Gr. Eng.*, **1**, 23. https://doi.org/10.1007/s40891-015-0025-3.

Chen, W.F. and Liu, X.L. (1990), Limit analysis in soil mechanics. Amsterdam, Elsevier.

Chenari, M.J., Payan, M. and Ghasemi-Fare, O. (2023), "Nonisothermal failure envelopes of strip shallow foundations resting on partially saturated clay subjected to combined inclined and eccentric loadings", *Int. J. Geomech.*, **23**(1), https://doi.org/10.1061/(ASCE)GM.1943-5622.0002596.

Coulomb, C.A. (1776), "Essai sur une application des règles de maximis & minimis à quelques problèmes de statique à l'architecture. l'Imprimerie", *Mem. Acad. Roy. Div. Sav.*

Das, P.P. and Khatri, V.N. (2022), "Bearing capacity prediction of strip and ring footings embedded in layered sand", *Proc. Inst. Civ. Eng. - Geotech. Eng*., 1-18. https://doi.org/10.1680/jgeen.22.00071.

Dey, A.K., Dey, A. and Sukladas, S. (2017), "3 N formulation of the horizontal slice method in evaluating pseudostatic method for analysis of seismic active earth pressure", *Int. J. Geomech.*, **17**, 04016037. https://doi.org/10.1061/(asce)gm.1943-5622.0000662

Farshidfar, N., Keshavarz, A. and Mirhosseini, S.M. (2020), "Pseudo-static seismic analysis of reinforced soil slopes using the horizontal slice method", *Arab. J. Geosci.*, **13**. https://doi.org/10.1007/s12517-020-5269-0.

Fatehi, M., Hosseinpour, I., Jamshidi Chenari, R., Payan, M. and Javankhoshdel, S. (2023), "Deterministic seismic stability analysis of reinforced slopes using pseudo-static approach", *Iran J. Sci. Technol. Trans. Civ. Eng.*, **47**, 1025-1040. https://doi.org/10.1007/s40996-022-00970-2.

Fathipour, H., Bahmani Tajani, S., Payan, M., Chenari, R.J. and Senetakis, K. (2022), "Influence of transient flow during infiltration and isotropic/anisotropic matric suction on the passive/active lateral earth pressures of partially saturated soils", *Eng. Geol.*, **310**, 106883. https://doi.org/10.1016/j.enggeo.2022.106883.

Fathipour, H., Payan, M. and Jamshidi Chenari, R. (2021a), "Limit analysis of lateral earth pressure on geosynthetic-reinforced retaining structures using finite element and second-order cone programming", *Comput. Geotech.*, **134**, 104119. https://doi.org/10.1016/j.compgeo.2021.104119.

Fathipour, H., Payan, M., Jamshidi Chenari, R. and Senetakis, K. (2021b), "Lower bound analysis of modified pseudo-dynamic lateral earth pressures for retaining wall-backfill system with depth-varying damping using FEM-Second order cone programming", *Int. J. Numer Anal. Method. Geomech.*, **45**, 2371-2387. https://doi.org/10.1002/nag.3269.

Fathipour, H., Payan, M., Safardoost Siahmazgi, A., Jamshidi Chenari, R. and Senetakis, K. (2023a), "Numerical study on the bearing capacity of strip footing resting on partially saturated soil subjected to combined vertical-horizontal-moment loading", *Eur. J. Environ. Civ. Eng.*, **27**, 1317-1350. https://doi.org/10.1080/19648189.2022.2080769.

Fathipour, H., Safardoost Siahmazgi, A., Payan, M. and Jamshidi Chenari, R. (2020), "Evaluation of the lateral earth pressure in unsaturated soils with finite element limit analysis using second-order cone programming", *Comput. Geotech*., **125**, 103587. https://doi.org/10.1016/j.compgeo.2020.103587.

Fathipour, H., Siahmazgi, A.S., Payan, M., Veiskarami, M. and Jamshidi Chenari, R. (2021c), "Limit analysis of modified pseudodynamic lateral earth pressure in anisotropic frictional medium using finite-element and second-order cone programming", *Int. J. Geomech*., **21**, 1-15. https://doi.org/10.1061/(asce)gm.1943-5622.0001924.

Fathipour, H., Tajani, S.B., Payan, M., Chenari, R.J. and Senetakis, K. (2023b), "Impact of transient infiltration on the ultimate bearing capacity of obliquely and eccentrically loaded strip footings on partially saturated soils", *Int. J. Geomech*., **23**. https://doi.org/10.1061/IJGNAI.GMENG-7463.

Fausett, L (1994), Fundamentals of Neural Network. Prentice Hall, Hoboken.

Feng, X. and Jimenez, R. (2015), "Predicting tunnel squeezing with incomplete data using Bayesian networks", *Eng. Geol.*, **195**, 214-224. https://doi.org/10.1016/j.enggeo.2015.06.017.

Fredlund, D.G., Morgenstern, N.R. and Widger, R.A. (1978), "The shear strength of unsaturated soils", *Can Geotech. J*., **15**, 313-321. https://doi.org/10.1139/t78-029.

Ganesh, R. and Rajesh, S. (2021), "Analytical solution to estimate the point of application of resultant passive earth thrust against unsaturated retaining structures", *Geomech. Geoeng*., **16**, 509-516. https://doi.org/10.1080/17486025.2019.1680880.

Garson, G.D. (1991), "Interpreting neural network connection weights", *AI Expert Arch*., **6**, 46-51

Ghanbari, A. and Ahmadabadi, M. (2010), "Pseudo-dynamic active earth pressure analysis of inclined Retaining walls using horizontal slices method", *Sci. Iran*, **17**, 118-130.

Gnananandarao, T., Khatri, V.N. and Dutta, R.K. (2020), "Prediction of bearing capacity of H shaped skirted footings on sand using soft computing techniques", *Arch. Mater. Sci. Eng*., **103**, 62-74. https://doi.org/10.5604/01.3001.0014.3356.

Goh, A.T.C., Kulhawy, F.H. and Chua, C.G. (2005), "Bayesian neural network analysis of undrained side resistance of drilled shafts", *J. Geotech. Geoenviron. Eng.*, **131**, 84-93. https://doi.org/10.1061/(ASCE)1090-0241(2005)131:1(84),

Hasthi, V., Nouman Amjad Raja, M., Hegde, A. and Kumar Shukla, S. (2022), "Experimental and intelligent modelling for predicting the amplitude of footing resting on geocell-reinforced soil bed under vibratory load", *Transp. Geotech.*, **35**, 100783. https://doi.org/10.1016/j.trgeo.2022.100783.

Kalinli, A., Acar, M.C. and Gündüz, Z. (2011), "New approaches to determine the ultimate bearing capacity of shallow foundations based on artificial neural networks and ant colony

optimization", *Eng. Geol.*, **117**, 29-38. https://doi.org/10.1016/j.enggeo.2010.10.002.

Kardani, N., Bardhan, A., Gupta, S., Samui, P., Nazem, M., Zhang, Y. and Zhou, A. (2022), "Predicting permeability of tight carbonates using a hybrid machine learning approach of modified equilibrium optimizer and extreme learning machine", *Acta Geotech.*, **17**, 1239-1255. https://doi.org/10.1007/s11440-021-01257-y

Khan, M.U.A., Shukla, S.K. and Raja, M.N.A. (2021), "Soil–conduit interaction: an artificial intelligence application for reinforced concrete and corrugated steel conduits", *Neural Comput. Appl.*, **33**, 14861-14885. https://doi.org/10.1007/s00521-021-06125-0.

Khodkari, N., Hamidian, P., Khodkari, H., Payan, M. and Behnood, A. (2024), "Predicting the small strain shear modulus of sands and sand-fines binary mixtures using machine learning algorithms", *Transp. Geotech.*, **44**, 101172. https://doi.org/10.1016/j.trgeo.2023.101172.

Kim, D., Kwon, K., Pham, K., Oh, J.Y. and Choi, H. (2022), "Surface settlement prediction for urban tunneling using machine learning algorithms with Bayesian optimization", *Automat. Constr.*, **140**, 104331. https://doi.org/10.1016/j.autcon.2022.104331.

Kolathayar, S. and Ghosh, P. (2009), "Seismic active earth pressure on walls with bilinear backface using pseudo-dynamic approach", *Comput. Geotech.*, **36**, 1229-1236. https://doi.org/10.1016/j.compgeo.2009.05.015.

Kolathayar, S. and Ghosh, P. (2011), "Seismic passive earth pressure on walls with bilinear backface uUsing pseudo-dynamic approach", *Geotech. Geol. Eng.*, **29**, 307-317. https://doi.org/10.1007/s10706-010-9377-6.

Kuo, Y.L., Jaksa, M.B., Lyamin, A.V. and Kaggwa, W.S. (2009), "ANN-based model for predicting the bearing capacity of strip footing on multi-layered cohesive soil", *Comput. Geotech.*, **36**, 503-516. https://doi.org/10.1016/j.compgeo.2008.07.002.

Li, Z.W. and Yang, X.L. (2019), "Active earth pressure from unsaturated soils with different water levels", *Int. J. Geomech.*, **19**, 1-10. https://doi.org/10.1061/(asce)gm.1943-5622.0001471.

Liang, W., Zhao, J., Li, Y., Zhang, C.G. and Wang, S. (2012), "Unified solution of Coulomb's active earth pressure for unsaturated soils without crack", *Appl. Mech. Mater.*, **170-173**, 755-761. https://doi.org/10.4028/www.scientific.net/AMM.170-173.755

Lu, N., Godt, J.W. and Wu, D.T. (2010), "A closed-form equation for effective stress in unsaturated soil", *Water Resour. Res.*, **46**. https://doi.org/10.1029/2009WR008646

Lu, N. and Griffiths, D.V. (2004), "Profiles of steady-state suction stress in unsaturated soils", *J. Geotech. Geoenviron. Eng.*, **130**, 1063-1076. https://doi.org/10.1061/(ASCE)1090-0241(2004)130:10(1063).

Lu, N. and Likos, W.J. (2006), "Suction stress characteristic curve for unsaturated soil", *J. Geotech. Geoenviron. Eng.*, **132**, 131-142. https://doi.org/10.1061/(asce)1090-0241(2006)132:2(131).

Maghferati, S.P., Jamshidi Chenari, R., Lajevardi, S.H., Payan, M. and Mirhosseini, S.M. (2023), "Seismic combined bearing capacity of strip footings on partially saturated soils using lower bound theorem of finite element limit analysis and second-order cone programming", *Comput. Geotech.*, **157**, 105327. https://doi.org/10.1016/j.compgeo.2023.105327

Menon, V. and Kolathayar, S. (2024), "Optimizing nailing parameters for hybrid retaining systems using supervised learning regression models", *Multiscale Multidiscip. Model. Exp. Des.*, https://doi.org/10.1007/s41939-024-00417-3

Mirmoazen, S.M., Lajevardi, S.H., Mirhosseini, S.M., Payan, M. and Chenari, R.J. (2021), "Active lateral earth pressure of geosynthetic-reinforced retaining walls with inherently anisotropic frictional backfills subjected to strip footing loading", *Comput. Geotech.*, 137, 3-4. https://doi.org/10.1016/j.compgeo.2021.104302

Mirmoazen, S.M., Lajevardi, S.H., Mirhosseini, S.M., ayan, M. and Chenari, R.J. (2022), "Limit analysis of lateral earth pressure on geosynthetic-reinforced retaining structures subjected to strip footing loading using finite element and second-order cone programming", *Iran J. Sci. Technol. Trans. Civ. Eng.*, **46**, 3181–3192. https://doi.org/10.1007/s40996-021-00793-7.

Momeni, E., Nazir, R., Armaghani, D.J. and Maizir, H. (2015), "Application of artificial neural network for predicting shaft and tip resistances of concrete piles", *Earth. Sci. Res. J.*, **19**, 85-93. https://doi.org/10.15446/esrj.v19n1.38712.

Ngamkhanong, C., Keawsawasvong, S., Jearsiripongkul, T., Cabangon, L.T., Payan, M., Sangjinda, K., Banyong, R. and Thongchom, C. (2022), "Data-driven prediction of stability of rock tunnel heading: An application of machine learning mModels", *Infrastruct.*, **7**(11), 148. https://doi.org/10.3390/infrastructures7110148.

Nguyen, H., Moayedi, H., Foong, L.K., Al Najjar, H.A>H., Jusoh, W.A.W., Rashid, A.S.A. and Jamali, J. (2020), "Optimizing ANN models with PSO for predicting short building seismic response", *Eng. Comput.*, **36**, 823-837. https://doi.org/10.1007/s00366-019-00733-0.

Nguyen, T., Ly, K.D., Nguyen-Thoi, T., Nguyen, B.P. and Doan, N.P. (2022), "Prediction of axial load bearing capacity of PHC nodular pile using Bayesian regularization artificial neural network", *Soils Found.*, **62**, 101203. https://doi.org/10.1016/j.sandf.2022.101203.

Ning, L. and William, L. (2004), Unsaturated Soil Mechanics.

Nouzari, M.A., Jamshidi Chenari, R., Payan, M. and Pishgar, F. (2021a), "Pseudo-static seismic bearing capacity of shallow foundations in unsaturated soils employing limit equilibrium method", *Geotech. Geol. Eng.*, **39**, 943-956. https://doi.org/10.1007/s10706-020-01535-8.

Nouzari, M.A., Jamshidi Chenari, R., Payan, M. and Pishgar, F. (2021b), "Pseudo-static seismic bearing capacity of shallow foundations in unsaturated soils employing limit equilibrium method", *Geotech, Geol, Eng.*, **39**, 943-956. https://doi.org/10.1007/s10706-020-01535-8.

Olden, J.D. and Jackson, D.A. (2002), "Illuminating the "black box": a randomization approach for understanding variable contributions in artificial neural networks", *Ecol. Modell.*, **154**, 135-150. https://doi.org/10.1016/S0304-3800(02)00064-9.

Payan, M., Fathipour, H., Hosseini, M., Chenari, R.J. and Shiau, J.S. (2022), "Lower bound finite element limit analysis of geo-structures with non-associated flow rule", *Comput. Geotech.*, **147**, 104803. https://doi.org/10.1016/j.compgeo.2022.104803.

Rahaman, O. and Raychowdhury, P. (2017), "Seismic active earth pressure on bilinear retaining walls using a modified pseudo-dynamic method", *Int. J. Geo-Eng.*, **8**(6). https://doi.org/10.1186/s40703-017-0040-4.

Raja, M.N.A. and Shukla, S.K. (2021a), "Predicting the settlement of geosynthetic-reinforced soil foundations using evolutionary artificial intelligence technique", *Geotext. Geomembranes*, **49**, 1280-1293. https://doi.org/10.1016/j.geotexmem.2021.04.007.

Raja, M.N.A. and Shukla, S.K. (2021b), "Predicting the settlement of geosynthetic-reinforced soil foundations using evolutionary artificial intelligence technique", *Geotext. Geomembranes*, **49**, 1280-1293. https://doi.org/10.1016/j.geotexmem.2021.04.007.

Raja, M.N.A., Shukla, S.K. and Khan, M.U.A. (2022), "An intelligent approach for predicting the strength of geosynthetic-reinforced subgrade soil", *Int. J. Pavement Eng.*, **23**, 3505-3521. https://doi.org/10.1080/10298436.2021.1904237.

Rajesh, S. and Ganesh, R. (2022), "Analytical solution for the action of seismic active earth pressures of unsaturated backfills behind inclined walls", *Lecture Notes in Civil Engineering*, 17-

31.
Reeves, C.R. (1993), Modern heuristic techniques for combinatorial problems, McGraw-Hill, UK
Sadrekarimi, A. (2010), "Pseudo-static lateral earth pressures on broken-back retaining walls", *Can Geotech. J.*, **47**, 1247-1258. https://doi.org/10.1139/T10-025.
Sadrekarimi, A. (2017), "Seismic distress of broken-back gravity retaining walls", *J. Geotech. Geoenviron. Eng.*, **143**, 04016118. https://doi.org/10.1061/(ASCE)GT.1943-5606.0001612.
Sadrekarimi, A., Ghalandarzadeh, A. and Sadrekarimi, J. (2008), "Static and dynamic behavior of hunchbacked gravity quay walls", *Soil Dyn. Earthq. Eng.*, **28**, 99-117. https://doi.org/10.1016/j.soildyn.2007.05.004.
Sahoo, J.P. and Ganesh, R. (2018), "Active earth pressure on retaining walls with unsaturated soil backfill", *Sustain. Civ. Infrastruct.*, 1-19. https://doi.org/10.1007/978-3-319-63889-8_1.
Sangdeh, M.K., Salimi, M., Khansar, H.H., Dokaneh, M., Zanganeh Ranjbar, P., Payan, M. and Arabani, M. (2024), "Predicting the precipitated calcium carbonate and unconfined compressive strength of bio-mediated sands through robust hybrid optimization algorithms", *Transp. Geotech*., **46**, 101235. https://doi.org/10.1016/j.trgeo.2024.101235.
Santhoshkumar, G. and Ghosh, P. (2020), "Seismic stability of a broken-back retaining wall using adaptive collapse mechanism", *Int. J. Geomech.*, 20:04020154. https://doi.org/10.1061/(asce)gm.1943-5622.0001786.
Shahgholi, M., Fakher, A. and Jones, C.J.F.P. (2001), "Horizontal slice method of analysis", *Geotechnique*, **51**, 881-885. https://doi.org/10.1680/geot.2001.51.10.881.
Shahrokhabadi, S., Vahedifard, F., Ghazanfari, E. and Foroutan, M. (2019a), "Earth pressure profiles in unsaturated soils under transient flow", *Eng. Geol*., **260**, 105218. https://doi.org/10.1016/j.enggeo.2019.105218.
Shahrokhabadi, S., Vahedifard, F., Ghazanfari, E. and Foroutan, M. (2019b), "Earth pressure profiles in unsaturated soils under transient flow", *Eng. Geol.*, **260**, 105218. https://doi.org/10.1016/j.enggeo.2019.105218.
Stanier, S. and Tarantino, A. (2010), "Active earth force in 'cohesionless' unsaturated soils using bound theorems of plasticity", *Unsaturated Soils*. CRC Press, 1081-1086.
Terzaghi, K. (1943), Theoretical Soil Mechanics, John Wiley & Sons, Inc., Hoboken, NJ, USA
Thottoth, S.R., Das, P.P. and Khatri, V.N. (2024a), "Prediction of compression capacity of under-reamed piles in sand and clay", *Multiscale Multidiscip. Model. Exp. Des.*, https://doi.org/10.1007/s41939-023-00331-0.
Thottoth, S.R., Khatri, V.N., Kolathayar, S., Keawsawasvong, S. and Lai, V.Q. (2024b), "Optimizing seismic earth pressure estimates for battered retaining walls using numerical methods and ANN", *Geotech. Geol. Eng*., **42**, 3307-3329. https://doi.org/10.1007/s10706-023-02731-y
Vahedifard, F., Leshchinsky, B.A., Mortezaei, K. and Lu, N. (2015), "Active earth pressures for unsaturated retaining structures", *J. Geotech. Geoenviron. Eng*., **141**(11), 236. https://doi.org/10.1061/(ASCE)GT.1943-5606.0001356.
Vo, T. and Russell, A.R. (2014), "Slip line theory applied to a retaining wall–unsaturated soil interaction problem", *Comput. Geotech.*, **55**, 416-428. https://doi.org/10.1016/j.compgeo.2013.09.010.
Wang, L., Sun, D. and Li, L. (2019), "3D stability of partially saturated soil slopes after rapid drawdown by a new layer-wise summation method", *Landslides*, **16**, 295-313. https://doi.org/10.1007/s10346-018-1081-2.
Wang, L., Sun, D., Yao, Y., Wu, L. and Xu, Y. (2020), "Kinematic limit analysis of three-dimensional unsaturated soil slopes reinforced with a row of piles", *Comput. Geotech*., **120**, 103428. https://doi.org/10.1016/j.compgeo.2019.103428.
Xiao, F. and Zhao, Z. (2019), "Evaluation of equivalent hydraulic aperture (EHA) for rough rock fractures", *Can Geotech. J.*, **56**, 1486-1501. https://doi.org/10.1139/cgj-2018-0274.
Yang, X.L. and Chen, H. (2021), "Seismic analysis of 3D active earth pressure for unsaturated backfill.", *Transp. Geotech.*, **30**, 100593. https://doi.org/10.1016/j.trgeo.2021.100593.
Zhang, C., Zhao, J., Zhang, Q. and Xu, F. (2010), "Unified solutions for unsaturated soil shear strength and active earth pressure", *Experimental and Applied Modeling of Unsaturated Soils*. American Society of Civil Engineers, Reston, VA, 218-224
Zhang, W., Wu, C., Zhong, H., Li, Y. and Wang, L. (2021), "Prediction of undrained shear strength using extreme gradient boosting and random forest based on Bayesian optimization", *Geosci. Front*, **12**(1), 469-477. https://doi.org/10.1016/j.gsf.2020.03.007.
Zhao, L.H., Luo, Q., Li, L., Yang, F. and Yang, X.L. (2009), "The upper bound "Calculation of Passive Earth Pressure Based on Shear Strength theory of unsaturated soil", *Slope Stability, Retaining Walls, and Foundations*. American Society of Civil Engineers, Reston, VA, 151-157.
Zurada, J.M. (1992), Introduction to Artificial Neural Systems. West Group.

JS